

Monte Carlo study of very weak first-order transitions in the three-dimensional Ashkin-Teller model

Peter Arnold and Yan Zhang

Department of Physics, University of Washington, Seattle, Washington 98195

(October, 1996)

Abstract

We propose numerical simulations of the Ashkin-Teller model as a foil for theoretical techniques for studying very weakly first-order phase transitions in three dimensions. The Ashkin-Teller model is a simple two-spin model whose parameters can be adjusted so that it has an arbitrarily weakly first-order phase transition. In this limit, there are quantities characterizing the first-order transition which are universal: we measure the relative discontinuity of the specific heat, the correlation length, and the susceptibility across the transition by Monte Carlo simulation.

This report was prepared as an account of work sponsored by the United States Government. Neither the United States nor the United States Department of Energy, nor any of their employees, nor any of their contractors, subcontractors, or their employees, makes any warranty, express or implied, or assumes any legal liability or responsibility for the product or process disclosed, or represents that its use would not infringe privately-owned rights. By acceptance of this article, the publisher and/or recipient acknowledges the U.S. Government's right to retain a non-exclusive, royalty-free license in and to any copyright covering this paper.

I. INTRODUCTION

One of the modern scenarios for explaining the baryon asymmetry of the universe depends on the nature of the electroweak phase transition in the early universe. The scenario requires the transition to be first-order, but in some cases of interest the transition is sufficiently weak and near-critical that simple perturbative expansions around mean field theory are not well-behaved. The study of this cosmological application has spawned a general renewal of interest in techniques for studying critical or near-critical phase transitions: techniques that have a two decade history in condensed matter physics. The Ising model is the canonical example of a three-dimensional system with a second-order phase transition and has been well studied both numerically and theoretically. There has not, however, been a comparable amount of attention paid to any canonical example of weak, near-critical first-order transitions. A simple two-spin generalization of the Ising model that can provide such a canonical example—a testbed for theoretical techniques for treating very weakly first-order transitions in three dimensions—is the Ashkin-Teller model. By tuning parameters in this model, one can obtain first-order transitions that are arbitrarily weak.

A full discussion of our motivation for studying this model, and its similarities and dissimilarities with the electroweak phase transition, is given in ref. [1]. In the present paper, we will study the relative discontinuity of various physical quantities across the first-order transition. In particular, we measure the ratios C_+/C_- , ξ_+/ξ_- , and χ_+/χ_- where C_+ , ξ_+ , χ_+ are the specific heat, correlation length, and susceptibility in the disordered (high-temperature) phase and C_- , ξ_- , and χ_- are the same in the ordered (low-temperature) phase. These ratios are universal in the limit that the first-order transition is arbitrarily weak and provide a set of tests against which to measure theoretical techniques for studying weakly first-order transitions. In particular, a comparison of our numerical results against the predictions of ϵ -expansion methods [2,3] may be found in ref. [1].

In the remainder of this introduction, we review the Ashkin-Teller model and then present our final results. We will review the parameter x of the Ashkin-Teller model whose $x \rightarrow 0^+$

limit yields arbitrarily weakly first-order transitions. In sec. II, we give a broad overview of our method for making measurements in the two phases and for determining the transition temperature. In sec. III, we present our measured ratios for an assortment of values of x ; discuss how C_{\pm} , ξ_{\pm} , and χ_{\pm} should scale at small x ; explain how finite- x corrections to our $x \rightarrow 0^+$ ratios should scale with x ; and discuss our procedure for extracting the $x \rightarrow 0^+$ limit. In sec. IV, we discuss the details that went into the individual measurements at each x such as our procedure for measuring susceptibilities and correlation lengths, our assessment of finite volume errors, and uncertainties in the transition temperature and their effect on our measurements.

A. Review of the Ashkin-Teller Model

The (symmetric) Ashkin-Teller model [4] is a system with two Ising spins s_i and t_i per lattice site i , with the nearest-neighbor interaction

$$\beta H = -\beta \sum_{\langle ij \rangle} (s_i s_j + t_i t_j + x s_i t_i s_j t_j), \quad s_i, t_j = \pm 1. \quad (1.1)$$

Special cases of interest include $x=0$, which corresponds to two decoupled Ising models, and $x=1$, which can be rewritten as

$$\beta H(x=1) = -4\beta \sum_{\langle ij \rangle} \left(\delta_{s_i s_j} \delta_{t_i t_j} - \frac{1}{4} \right) \quad (1.2)$$

and is equivalent to the 4-state Potts model [5]. The phase diagram of the model in three dimensions on a simple cubic lattice is sketched in fig. 1 [6]. The portion of this diagram we will focus on is the neighborhood of the Ising tri-critical point at $x=0$. By studying arbitrarily small but positive values of x , we can study arbitrarily weak first-order phase transitions. Our goal will be to extract ratios such as

$$\lim_{x \rightarrow 0^+} \frac{C_+}{C_-} \equiv \lim_{x \rightarrow 0^+} \frac{\lim_{\beta \rightarrow \beta_t^-} C}{\lim_{\beta \rightarrow \beta_t^+} C}, \quad (1.3)$$

where $\beta_t = \beta_t(x)$ is the inverse transition temperature for a given value of x .

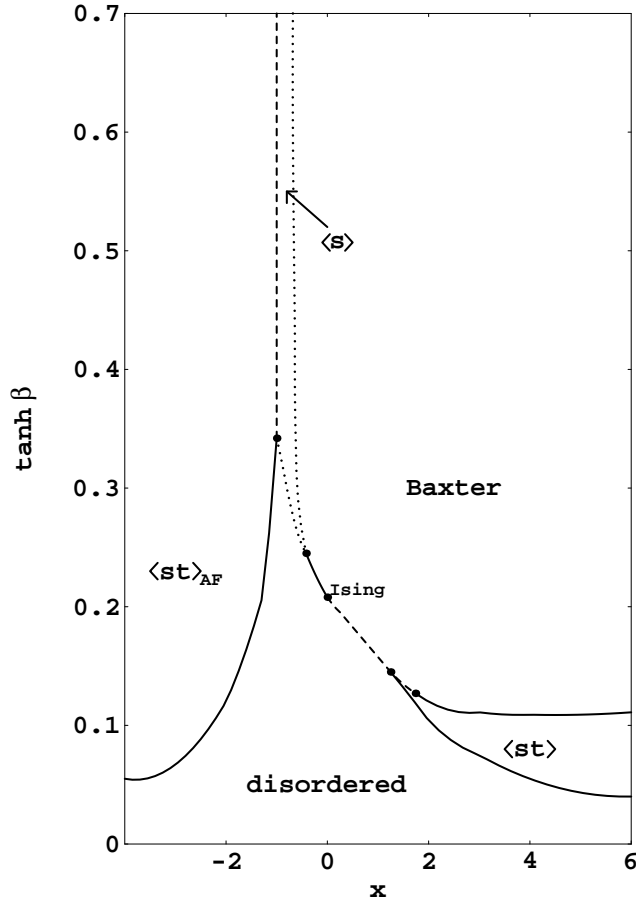


FIG. 1. Believed phase diagram of three-dimensional Ashkin-Teller model on a simple cubic lattice, taken from ref. [6], where it was extracted from series analysis and Monte Carlo data. Dashed and solid lines indicate first and second-order transitions respectively. Dotted lines indicate cases where the nature of the transition has not been unambiguously determined. The phases are labeled disordered ($\langle s \rangle = \langle t \rangle = 0$); Baxter (ferromagnetic with $\langle s \rangle$, $\langle t \rangle$, and $\langle st \rangle$ non-zero); “ $\langle st \rangle$ ” (where $\langle st \rangle$ is ferromagnetically ordered but $\langle s \rangle = \langle t \rangle = 0$); “ $\langle st \rangle_{AF}$ ” (the same but anti-ferromagnetically ordered); and “ $\langle s \rangle$ ” (where either $\langle s \rangle$ or $\langle t \rangle$ is ferromagnetically ordered but the other is not and $\langle st \rangle = 0$.)

For generic values of the parameter x , the internal symmetry group of the model is that of a square, D_4 , acting on the spin states $(s, t) = (++)$, $(+-)$, $(--)$, $(-+)$. The line $x=0$ is a line of enhanced symmetry: the translation symmetry decouples for the s and t spins.¹ (A simple continuum model with the same long-distance degrees of freedom and symmetries is the cubic anisotropy model, a two-scalar field theory discussed in refs. [1–3,7,8].)

B. Final results

Our final results for the universal ratios are²

$$\lim_{x \rightarrow 0^+} \frac{C_+}{C_-} = 0.071(8), \quad (1.4)$$

$$\lim_{x \rightarrow 0^+} \frac{\xi_+}{\xi_-} = 1.6(2), \quad (1.5)$$

$$\lim_{x \rightarrow 0^+} \frac{\chi_+}{\chi_-} = 4.0(6), \quad (1.6)$$

where the error estimate on the last result should be taken with a grain of salt (see sec. III C for details). The susceptibility χ is formally defined in the infinite-volume limit by adding a source term $-\sum_i \mathbf{h} \cdot \mathbf{S}_i$ to βH , where $\mathbf{S} \equiv (s, t)$, and then taking

$$\chi = \frac{1}{2} \lim_{\mathbf{h} \rightarrow 0} \sum_a \frac{d}{dh_a} \langle S_a \rangle. \quad (1.7)$$

As an incidental consequence of our work, we also have what is, to our knowledge, the best measurement of the transition temperature of the 4-state Potts model ($x=1$) in three dimensions:

$$\beta_t(4\text{-state Potts}) = \begin{cases} 0.157154(4), & \text{simple cubic;} \\ 0.113752(5), & \text{body-centered cubic;} \end{cases} \quad (1.8)$$

¹ This makes the Ising point a particularly attractive multi-critical point to study because we know it's value of x in advance. Other multi-critical points would first require a numerical search for the corresponding multi-critical value x_c of x before we could proceed to numerically extract the limit $x \rightarrow x_c$ of ratios analogous to (1.3).

² Due to an improvement in our method of error analysis prior to publication, the numbers given here are slightly, but not significantly, different than those originally reported in ref. [1].

where β is normalized according to (1.2). For comparison, earlier values determined by Monte Carlo and series analysis are given in Table I. The series estimate of ref. [11] for body-centered cubic (BCC) lattices is off by roughly thrice their estimated error.

	$\beta_t(x=1)$	
	simple cubic	BCC
Monte Carlo, ref. [9]	0.158	
Monte Carlo, ref. [10]	$\simeq 0.15694$	
series, ref. [11]	0.162(2)	0.1176(13)
series, ref. [12]	0.161(3)	

TABLE I. Summary of previous Monte Carlo and series analysis results for β_t in the 4-state Potts model ($x=1$) in three dimensions. The Monte Carlo references do not quote error estimates. Note that our convention (1.2) for β differs from the usual one by a factor of 4.

II. OUTLINE OF CALCULATIONAL METHOD

Our lattices are simple cubic with helical boundary conditions (periodic except for a twist) and range in sizes up to 480×120^2 . In principle, it would be nice to verify the universality of $x \rightarrow 0^+$ ratios such as C_+/C_- by repeating the calculation on another lattice type, such as body-centered cubic. However, we have only made limited exploration of BCC lattices, and our data for this case is relegated to Appendix C.

We interlace two different update algorithms: a simple heatbath algorithm and a cluster-update algorithm.³ The cluster-update algorithm is a simple generalization of the usual cluster-update algorithms for $O(n)$ systems [13] and is described in Appendix A.

Our basic method for extracting our results is best outlined with a specific example: the specific heat ratio C_+/C_- . The first step is to measure C_+/C_- at fixed values of x , so

³ But some of our data was generated by heatbath only or by cluster only.

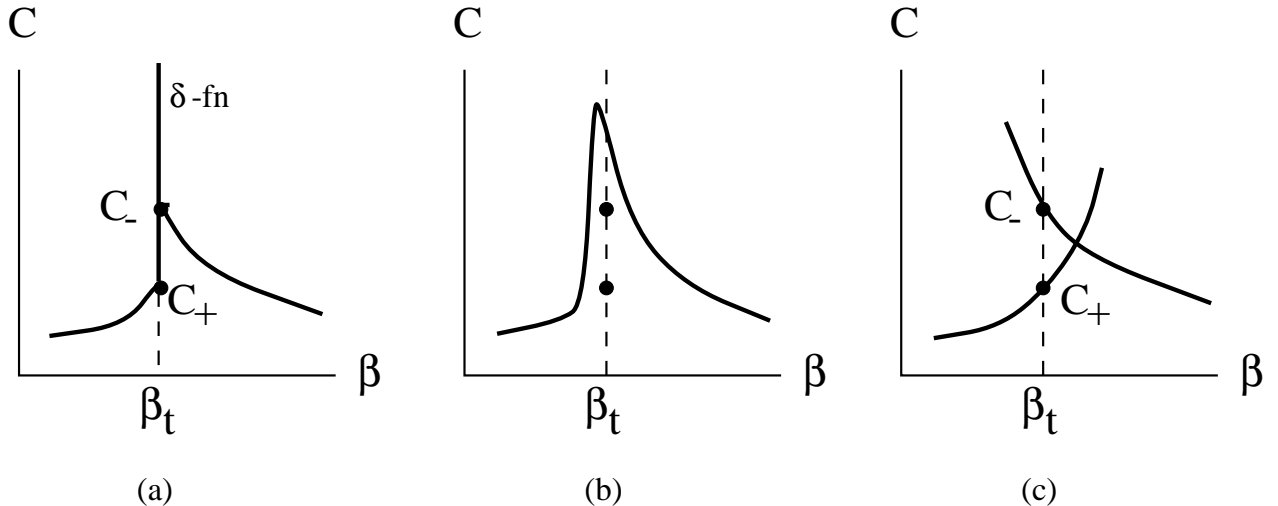


FIG. 2. Specific heat vs. β at fixed x for (a) infinite volume, (b) finite volume, (c) finite-time numerical simulations in large volume. The δ -function in (a) at β_t represents the latent heat. In all cases, β_t represents the true, infinite-volume transition temperature.

that we can later extract the $x \rightarrow 0^+$ limit. Fig. 2a qualitatively sketches the dependence of specific heat on inverse temperature β for fixed x . In finite volume, the latent heat δ -function at the transition temperature broadens out into a finite-width peak as in fig. 2b. If we actually measured this peak in numerical simulations, we would have to attack the problem of how to extract C_+ and C_- from beneath the peak. However, the lattices we work on are large enough that the mixing time between the two phases at the transition is very long compared to the duration of our simulations.⁴ Our results therefore have the form of fig. 2c: there is a range of temperatures, around the transition temperature, in which our simulation sits in either the ordered or disordered phase depending on whether we start with ordered or disordered initial conditions. The problem of extracting C_+ and C_- now becomes the problem of determining the inverse transition temperature β_t .

We determine the transition temperature by working on asymmetric lattices of size $L \times T \times T$ with $L \geq T$. We divide the L dimension in half, and we start the lattice in the

⁴ This is not an accident. The cleanest way to eliminate systematic errors from finite-volume effects is to work in volumes V large compared to the correlation volume V_ξ . But, at the transition temperature, the mixing time grows exponentially with V/V_ξ .

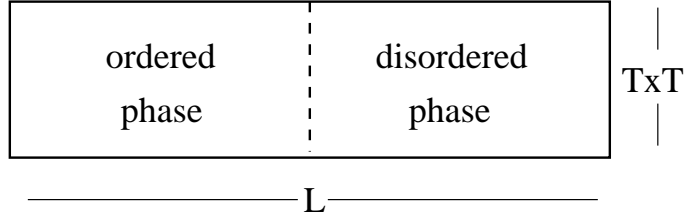


FIG. 3. Initial conditions used on asymmetric lattices for determining the transition temperature.

ordered phase in one half and the disordered phase in the other, as depicted in fig. 3. Next we evolve the system with our Monte Carlo update procedure. The domain walls will feel a net pressure to expand the phase with the lowest free energy. By tracking whether the system eventually evolves into the ordered or disordered phase, and finding the value of β where the favored phase changes, one determines the transition temperature. The story is a little more complicated, however. Exactly at the transition temperature, neither phase is favored and the domain walls will random walk until, randomly, they collapse the system into one phase or the other. Fig. 4 shows an example from our simulations of collapsing into either phase at the transition temperature. Slightly away from the transition temperature, there will be a slight bias to the random walks, but there will still be some chance of ending in the disfavored phase. The probability of ending up in one particular phase, say the ordered one, therefore has a dependence on temperature like that sketched in fig. 5a. It can be modeled as the solution to a classic problem from probability theory—the Gambler’s Ruin problem—which is described in Appendix B. Our technique for determining β_t is therefore to make multiple, independent runs at each temperature, in order to numerically extract the curve of fig. 5a, and then to fit for β_t . There is one more complication: even if the transverse dimension T is large compared to the correlation length, there are systematic errors in this procedure that have only power-law fall-off with increasing longitudinal dimension L , as depicted in fig. 5b. To get the best estimate of the transition temperature, we make the additional step of numerically extracting the $L \rightarrow \infty$ limit. A model for the finite L corrections is discussed in Appendix B and sec. IVD.

All of our calculations were carried out on a handful of SGI Indy R4600 workstations,

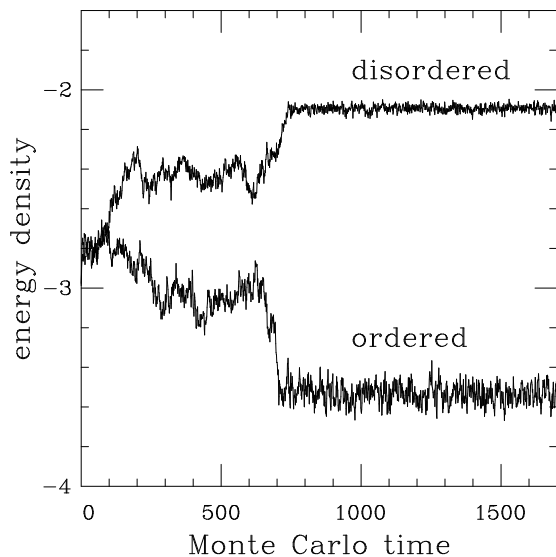


FIG. 4. Examples of evolution of energy density with Monte Carlo time starting from the mixed phase of fig. 3. The data is shown for $x=0.6$ on a 160×40^2 lattice near the transition temperature ($\beta = 0.180263$).

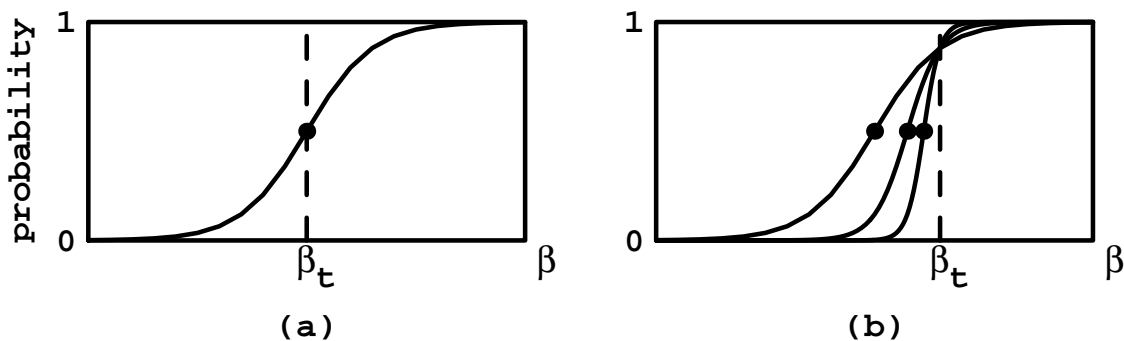


FIG. 5. (a) Probability of ending in the ordered phase vs. β when starting with mixed initial conditions; (b) the same but including finite L effects. The narrower curves correspond to larger L .

taking roughly 2 to 45 mins. per energy decorrelation time (depending on x) on an 80^3 lattice at the transition.

III. ANALYSIS OF DATA AND $x \rightarrow 0$

Table II and fig. 6 summarize our results for various ratios as a function of x on simple cubic lattices; table III shows in more detail the individual quantities that went into determining the ratios. We will explain in more detail our determination of these quantities in sec. IV. In this section, we will focus on understanding the small x behavior of the system and the extraction of the $x \rightarrow 0$ limits of the ratios. The errors quoted for our data are mostly statistical but include the systematic error from our uncertainty in the transition temperatures β_t . We estimate finite size effects to be no larger than our quoted total errors except possibly for our lowest value $x=0.3$ of x , where we do not have a very good estimate. For finite correlation length, the correlation length measured along edges of the lattice need not be exactly the same as that measured along diagonals, and so we have listed these cases separately. The $x \rightarrow 0^+$ ratio ξ_+/ξ_- in the two cases, however, should be the same.

x	C_+/C_-	ξ_+/ξ_-		χ_+/χ_-
		edge	diag.	
1.0	0.1228(19)	1.108(16) ^b	1.062(12) ^b	2.80(6)
0.8	0.122(3)	1.191(24) ^b	1.235(16) ^b	3.77(9)
0.6	0.109(3)	1.307(24) ^b	1.333(20) ^b	4.20(13)
0.5	0.103(3)	1.394(21) ^b	1.342(17) ^b	4.28(15)
0.3	0.088(8) ^a	1.45(7) ^{a,b}	1.41(8) ^{a,b}	3.8(5) ^a

TABLE II. Summary of relative discontinuities of specific heat, correlation length (along lattice edges and diagonals), and susceptibility vs. x . Errors include statistical errors and systematic errors due to the uncertainty in the determination of transition temperatures. Finite volume errors are not included and are estimated to be no larger than the total errors quoted above, except possibly for (a) the case $x=0.3$ where we do not have a good estimate of them. (See sec. IV for details.) (b) Errors for some correlation lengths are quite likely underestimated (see sec. IV B for details).

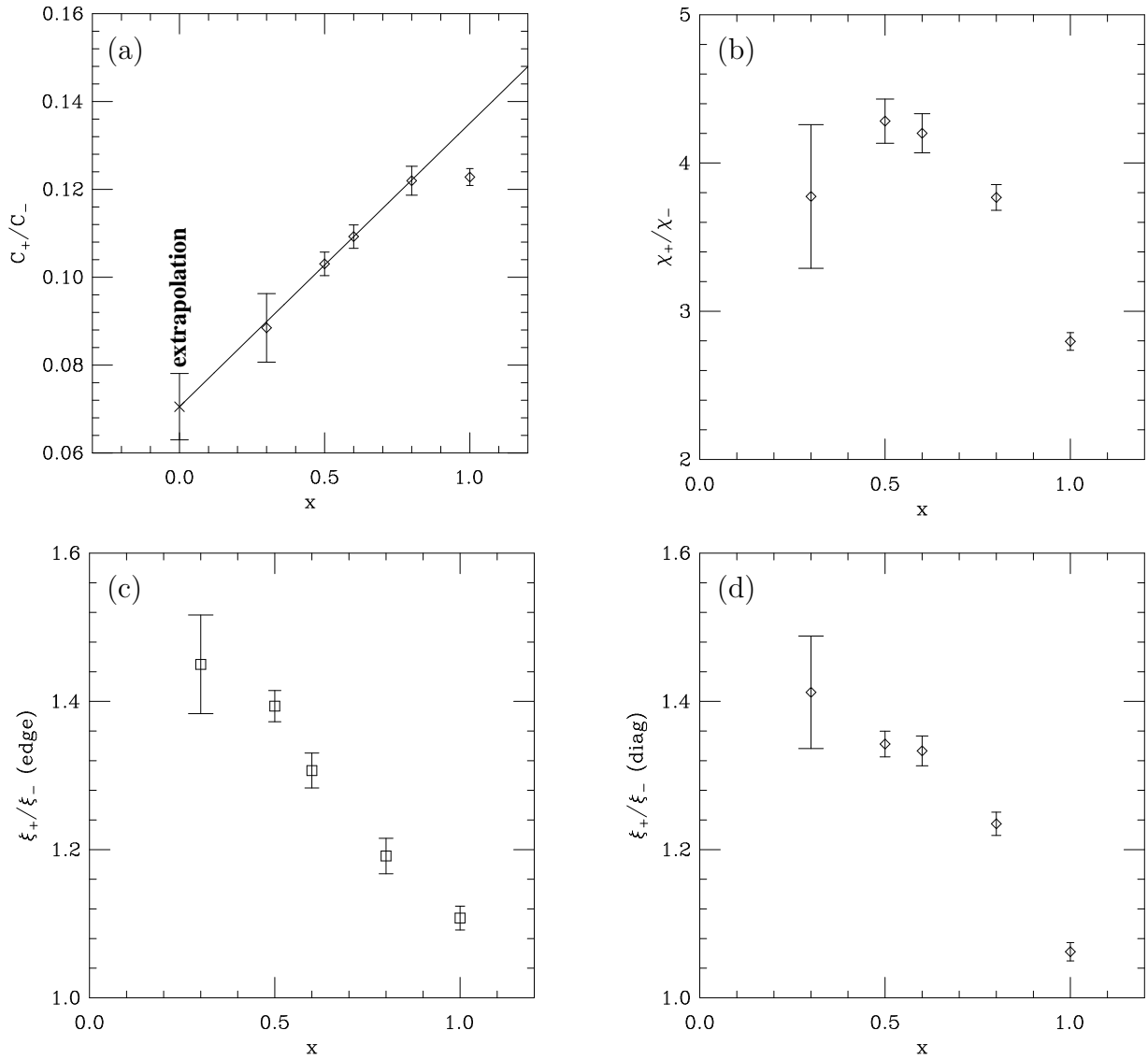


FIG. 6. Plots of the data in table II. For C_+/C_- , our best-fit interpolation and the extrapolated $x \rightarrow 0$ value are also shown (see sec. III C). Extrapolations of the other ratios are shown in fig. 10.

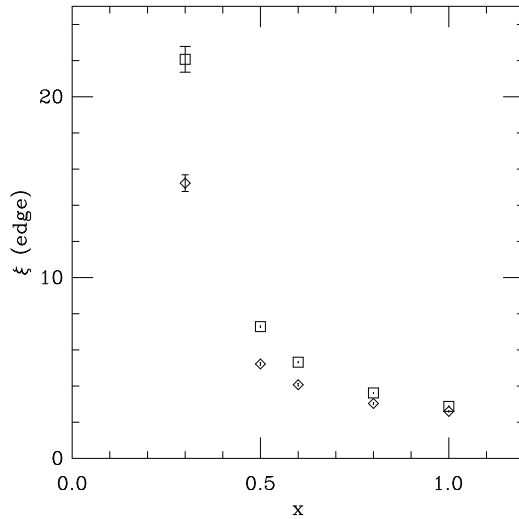


FIG. 7. The correlation length ξ^{edge} (measured along lattice edges) at the transition vs. x for the disordered phase (squares) and ordered phase (diamonds).

Our lowest value $x = 0.3$ of x is small in the sense that the transition is relatively weak: the correlation length at the transition is order 20 (see table III). Indeed, it is precisely the rapid growth of correlation length with decreasing x shown in fig. 7 (combined with the requirement that lattices be large compared to ξ to avoid transitions between the phases) that has prevented us from simulating even smaller x . However, despite the fact that $x = 0.3$ is “small,” the quality of our data in fig. 6 is such that, when attempting to extract the $x \rightarrow 0$ limits, we would clearly benefit tremendously from knowing *a priori* how the correction to the $x \rightarrow 0$ limit should scale for small x .

We shall first discuss how the individual quantities C_{\pm} , ξ_{\pm} , and χ_{\pm} scale with x . Then we turn to the scaling of the corrections to $x \rightarrow 0$ limit of ratios. Finally, armed with this analysis, we shall fit the data of fig. 6 as best we can.

x	β_t	ϵ_+	C_+	ξ_+^{edge}	ξ_+^{diag}	χ_+
		ϵ_-	C_-	ξ_-^{edge}	ξ_-^{diag}	χ_-
1	0.157154(4)	-2.2734(3)	1.663(13)	2.878(24)	2.985(14)	33.1(3)
		-4.6009(23)	13.54(18)	2.60(3)	2.81(3)	11.84(22)
0.8	0.168149(3)	-2.1552(4)	1.836(24)	3.62(3)	3.74(3)	51.9(9)
		-4.1726(23)	15.1(4)	3.04(6)	3.03(3)	13.78(20)
0.6	0.180272(3)	-2.0942(4)	2.33(3)	5.32(4)	5.47(5)	111(3)
		-3.5359(23)	21.3(4)	4.07(7)	4.10(5)	26.3(3)
0.5	0.186750(4)	-2.0797(3)	2.72(3)	7.28(5)	7.29(4)	203(3)
		-3.145(3)	26.4(6)	5.23(7)	5.43(6)	47.3(1.3)
0.3	0.2003659(15)	-2.0658(4)	5.16(21)	22.1(7)	21.6(8)	1730(180)
		-2.362(3)	58(4)	15.2(5)	15.3(6)	460(30)
0	0.221652(3) ^a					

TABLE III. Summary of inverse transition temperature β_t , energy density ϵ_{\pm} , specific heat density C_{\pm} , correlation length ξ_{\pm} , and susceptibility χ_{\pm} as a function of x on a simple cubic lattice. + and - denote the disordered and ordered phases, respectively, at the transition temperature. For some x , the errors on the correlation lengths are likely underestimated (see IV B for details). The $x=0$ Ising model β_t (a) is taken from ref. [14].

A. The Problem with Crossover Exponents

As we shall review below, one already knows how various dimensionful quantities, such as the correlation lengths ξ_{\pm} , should diverge as $x \rightarrow 0$. The divergence is characterized by crossover (or “tricritical”) exponents, *e.g.*

$$\xi_{\pm} \sim x^{-y}, \quad x \rightarrow 0. \quad (3.1)$$

In the case at hand, crossover exponents such as y may be determined from knowledge of Ising model critical exponents. In the Ising model, the scaling dimension of the nearest-

neighbor interaction in the Hamiltonian density is

$$\dim[s_i s_{i+\hat{e}}] = d - \frac{1}{\nu} = \frac{d}{2} - \frac{\alpha}{2\nu}, \quad (3.2)$$

where $d=3$ is the dimension of space. Now consider the scaling dimension of the interaction $(st)_i(st)_{i+\hat{e}}$ in the Ashkin-Teller model. For the purpose of understanding the crossover behavior at very small x , we can ignore the effect of the interaction itself on its scaling and instead consider the scaling dimension of the operator in the $x=0$ limit. Then the operator factorizes:

$$D \equiv \dim[(st)_i(st)_{i+\hat{e}}] = \dim[s_i s_{i+\hat{e}}] + \dim[t_i t_{i+\hat{e}}] = d - \frac{\alpha}{\nu}. \quad (3.3)$$

Deviation from Ising behavior will occur once this operator becomes important, which in our case means that the scale ξ of the first-order transition is related to the interaction's coefficient x by

$$x \sim \xi^{D-d} \sim \xi^{-\alpha/\nu}. \quad (3.4)$$

Using Ising scaling laws to get the power-law relationship of ξ with other quantities, one gets

$$\xi_{\pm} \sim x^{-\nu/\alpha} \sim x^{-5.7(3)}, \quad (3.5a)$$

$$\chi_{\pm} \sim x^{-\gamma/\alpha} \sim x^{-11.3(5)}, \quad (3.5b)$$

$$C_{\pm} \sim x^{-1}, \quad (3.5c)$$

where we have used the Ising model exponents [15]

$$\alpha \simeq 0.110(5), \quad \nu \simeq 0.6300(15), \quad \gamma \simeq 1.2405(15). \quad (3.6)$$

This result means, in the small x limit, that the correlation length and susceptibility should grow by factors of roughly 40–60 and 1500–3500 respectively when x is reduced by a factor of two! There is clearly no sign of such strong x dependence in the data of table III and fig. 7. A natural question now arises: Does this discrepancy indicate failure to reach the small x region of the Ashkin-Teller model and so make our $x \rightarrow 0$ limits for ratios suspect?

To address this question, one must first note that the origin of the strong x dependence in (3.5a-b) is the small value of the specific-heat exponent α in the Ising model. It is useful to formally consider what would have happened if α were arbitrarily small, or even zero. In Appendix D, we consider a simple model for the renormalization group flow where one can treat this explicitly. In the case $\alpha=0$, the relationship (3.4) generically becomes $x \sim 1/\ln(\xi)$, and one gets

$$\xi_{\pm} \sim e^{k\nu/x}, \quad (3.7a)$$

$$\chi_{\pm} \sim e^{k\gamma/x}, \quad (3.7b)$$

$$C_{\pm} \sim x^{-1}, \quad (3.7c)$$

$$\frac{C_+}{C_-} \sim \frac{\xi_+}{\xi_-} \sim \frac{\chi_+}{\chi_-} \sim 1, \quad (3.7d)$$

where k is some constant. For arbitrarily small but non-zero α , one finds exponential scaling (3.7a-b) of ξ and χ for moderately small x , but the power-law scaling form (3.5a-b) takes over when x drops below

$$x_1 \sim \frac{\alpha k}{\ln(1/\alpha k)}. \quad (3.8)$$

This threshold has no effect, however, on the extraction of the limits of ratios such as ξ_+/ξ_- . (See Appendix D for details.) So, though the formal limit $x \ll O(\alpha)$ is required to see correct scaling of ξ and χ , the weaker limit $x \ll O(1)$ is adequate for extracting the dimensionless ratios of interest. Our failure to see the correct scaling of ξ and χ in our numerical data should not, therefore, cause concern. Roughly, we expect that x should be small enough for computing ratios if the correlation length is large compared to the lattice spacing.

We can test the above assertions by examining relationships that don't depend on α and which should be satisfied for both the different scaling behaviors (3.5) and (3.7). One such relationship is that $\xi_{\pm} \sim \chi_{\pm}^{\nu/\gamma}$; therefore

$$\lim_{x \rightarrow 0^+} \frac{\ln \xi_{\pm}}{\ln \chi_{\pm}} = \frac{\nu}{\gamma}. \quad (3.9)$$

Fig. 8 shows this ratio of logarithms for our data and the theoretical limit (3.9). The data appears consistent with the limit. Another test is to check whether $x C_{\pm}$ approaches a

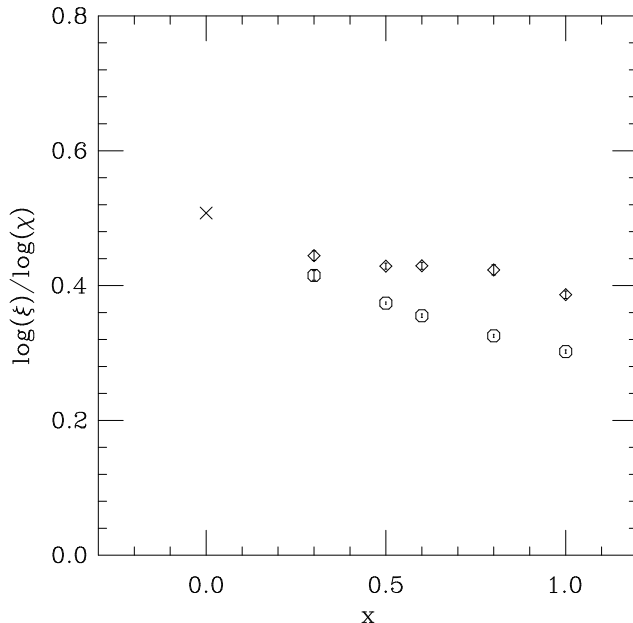


FIG. 8. A test of scaling: $\ln(\xi^{\text{edge}})/\ln(\chi)$ vs. x for the ordered phase (diamonds) and disordered phase (circles). The cross marks the theoretical value ν/γ for the $x \rightarrow 0$ limit. The corresponding graph for $\ln(\xi^{\text{diag}})/\ln(\chi)$ is visually almost identical.

constant as $x \rightarrow 0$. Fig. 9a shows $x C_+$ for our data, which looks reasonably good. Fig. 9b shows $x C_-$, which is reasonable except that the lowest x point is a bit high. (We shall see below that the approach to the $x \rightarrow 0$ limit should be linear at small x .)

B. Corrections to Scaling

In order to extrapolate $x \rightarrow 0$ limits for our ratios in fig. 6, it helps tremendously to know how the corrections to those limits scale with x . For simplicity, let us first ignore the small α issue. We have discussed in the previous section how, for very small x , the system has Ising behavior for distance scales up to order $\xi \sim x^{-\nu/\alpha}$. Corrections to scaling arise because there are irrelevant operators which have not quite scaled away for finite (but large) ξ . However, since the scaling of operators as $\xi \rightarrow \infty$ is determined by Ising behavior, we can extract the dimension of the most important such operator from well-known results in the Ising model: relative corrections to scaling behavior scale as $\xi^{-\omega}$, where ω is the Ising model exponent [15]

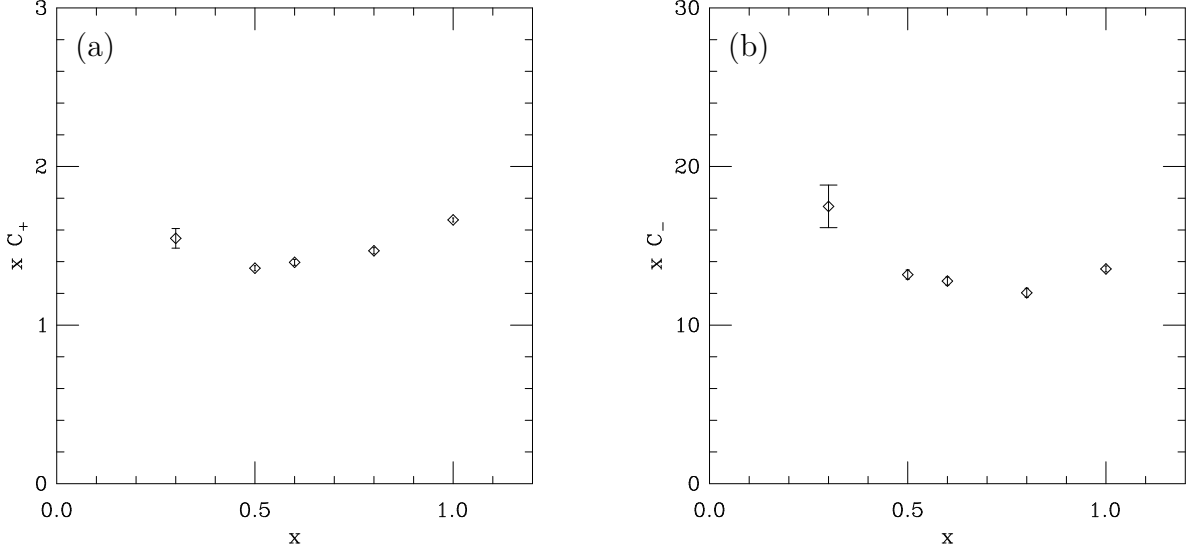


FIG. 9. A test of scaling: (a) $x C_+$ and (b) $x C_-$ vs. x .

$$\omega \simeq 0.79(3). \quad (3.10)$$

Translating ξ to x using (3.4), we then have, for example,

$$\chi_{\pm} \sim x^{-\gamma/\alpha} [1 + O(x^{\omega\nu/\alpha})], \quad (3.11)$$

$$\frac{\chi_+}{\chi_-} \sim O(1) + O(x^{\omega\nu/\alpha}). \quad (3.12)$$

Similarly,

$$\frac{\xi_+}{\xi_-} \sim O(1) + O(x^{\omega\nu/\alpha}). \quad (3.13)$$

The specific heat ratio is slightly different. In addition to the divergent $O(\xi^{\alpha/\nu}) = O(x^{-1})$ contribution from long-distance modes, the specific heat receives a direct contribution from short-distance modes that is analytic in ξ and is therefore $O(\xi^0) = O(x^0)$. This is much more important than the relative contribution discussed above and gives

$$C_{\pm} \sim O(\xi^{\alpha/\nu}) + O(\xi^0), \quad (3.14)$$

$$\frac{C_+}{C_-} \sim O(1) + O(x). \quad (3.15)$$

So far, we have discussed the correction to scaling in the limit of arbitrarily small x where everything scales with the correct Ising model exponents. But, as discussed in the previous section, the values of x we actually simulate are not small enough to reproduce relationships involving the small Ising exponent α . The scaling (3.15) of corrections to C_+/C_- is nonetheless in good shape because it does not depend on α and would hold even if α were zero. The scaling of corrections to other ratios can also be cast in a form that does not depend on α :

$$\frac{\chi_+}{\chi_-} \sim O(1) + O(\chi_{\pm}^{-\omega\nu/\gamma}). \quad (3.16a)$$

$$\frac{\xi_+}{\xi_-} \sim O(1) + O(\xi_{\pm}^{-\omega}). \quad (3.16b)$$

(3.15) and (3.16) are the forms we fit our data to in order to extract the $x \rightarrow 0$ limits of the ratios.

C. Extraction of $x \rightarrow 0$ limits from data

Now that we know how the corrections are supposed to scale, we can attempt to fit our data to the appropriate form. C_+/C_- is already plotted against the correct variable x in fig. 6 for a linear fit. In fig. 10, we show χ_+/χ_- and ξ_+/ξ_- plotted against $\chi_+^{-\omega\nu/\gamma}$ and $\xi_+^{-\omega}$ respectively, so that the fit should again be linear. Our procedure is to fit the largest set of points, working from the lowest x up, that yields a reasonable chi-squared.

For C_+/C_- , fitting the points $x \leq 0.8$ yields a freakishly high confidence level of 98% and produces our final result, eq. (1.4), for the $x \rightarrow 0$ limit. Adding the point $x = 1.0$ decreases the confidence level to 18% and would change the limit to 0.084(4). Because of its large uncertainty, our $x=0.3$ value has an almost negligible effect on the fit and our final result.

Next consider χ_+/χ_- . Fitting the three points $x \leq 0.6$ yields the best fit line (34% confidence level) shown in fig. 10a and our final result, eq. (1.6), for the $x \rightarrow 0$ limit. The systematic uncertainty in the values of the Ising critical exponents is included in our error estimate. Attempting to add the $x = 0.8$ point gives $\lim(\chi_+/\chi_-) = 4.8(3)$ with a fairly small

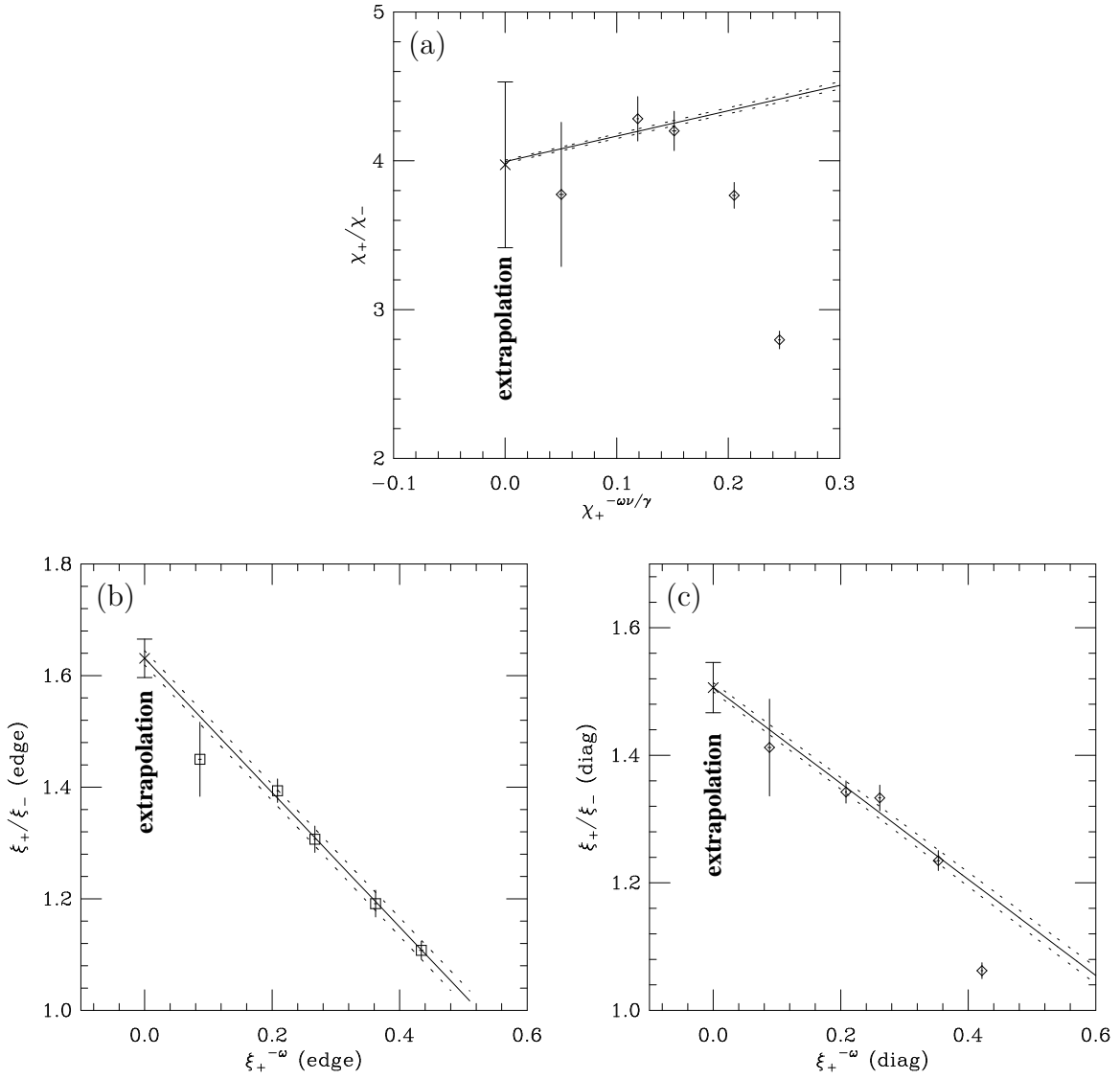


FIG. 10. Ratios vs. an appropriate scaling variable for corrections to the $x \rightarrow 0$ limit: (a) χ_+/χ_- vs. $\chi_+^{-\omega\nu/\gamma}$, and (b,c) ξ_+/ξ_- vs. $\xi_+^{-\omega}$ for edges and diagonals. Statistical uncertainties in the ordinates of the data points are too small to be seen. We have not shown for each data point the larger systematic uncertainties due to uncertainties in the Ising exponents (dominated by ω). The solid line is our best fit, and the $x=0$ value is our extrapolation. The dotted lines show how our best fit changes as ω is varied over the uncertainty indicated in (3.10), but this change is negligible in (a).

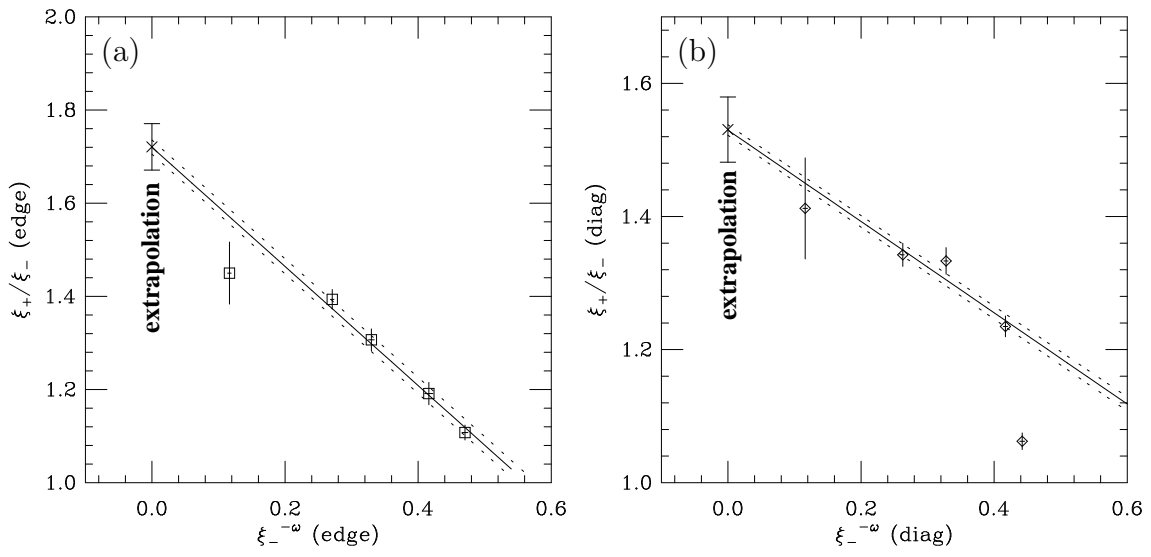


FIG. 11. ξ ratios vs. $\xi_-^{-\omega}$ instead of $\xi_+^{-\omega}$.

confidence level of 11%. We have parameterized corrections (3.16) to scaling by $\chi_+^{-\omega\nu/\gamma}$. An alternative choice would be $\chi_-^{-\omega\nu/\gamma}$, and we have used $\chi_+^{-\omega\nu/\gamma}$ simply because it is more straightforward to measure. If the fit is made against $\chi_-^{-\omega\nu/\gamma}$ instead of $\chi_+^{-\omega\nu/\gamma}$, the result for the limiting ratio is 4.0(5) and is consistent with the previous result. In any case, the situation is somewhat unsatisfactory to the extent that (1) we have fit only three points, and (2) one of those points is our lowest x value, $x = 0.3$, where we are less confident about finite volume errors (see sec. IV C).

In sec. IV B, we explain that our errors on extracting the correlation lengths may be underestimated. Our procedure for estimating our final error will simply be to interpolate the $x \rightarrow 0$ ratio in different ways that should in principle be equivalent. For $\xi_+^{\text{edge}}/\xi_-^{\text{edge}}$, we can obtain a reasonable (56% confidence level) fit vs. $(\xi_+^{\text{edge}})^{-\omega}$ with all our data points, shown in fig. 10b; for the diagonal ratio, we need to drop the $x=1.0$ point from the fit (improving the confidence level from $O(10^{-4}\%)$ to 36%). The results are

$$\lim_{x \rightarrow 0^+} \frac{\xi_+^{\text{edge}}}{\xi_-^{\text{edge}}} = 1.64(3), \quad \lim_{x \rightarrow 0^+} \frac{\xi_+^{\text{diag}}}{\xi_-^{\text{diag}}} = 1.51(4). \quad (3.17a)$$

Alternate interpolations using $\xi_-^{-\omega}$ are shown in fig. 11 and give

$$\lim_{x \rightarrow 0^+} \frac{\xi_+^{\text{edge}}}{\xi_-^{\text{edge}}} = 1.72(5), \quad \lim_{x \rightarrow 0^+} \frac{\xi_+^{\text{diag}}}{\xi_-^{\text{diag}}} = 1.53(5). \quad (3.17b)$$

The wide discrepancy of values in (3.17a) and (3.17b) should be taken as a reflection of our systematic errors in determining the correlation lengths and in extracting the $x \rightarrow 0$ limit. Our final result (1.5) has been chosen to span all of the above extrapolations.

Clearly it would be useful to have more good-quality data at small x , and, in particular, $x = 0.4$ suggests itself as a good candidate for future simulation. We estimate that $x = 0.4$ would take us 2-3 CPU years on our SGI Indys, and we have not yet attacked it. The most time-consuming part of the task is an accurate determination of the transition temperature.

IV. DETAILS

A. Susceptibilities

The definition (1.7) of the susceptibility is equivalent to

$$\chi = \frac{1}{2N} [\langle \tilde{\mathbf{S}}(0) \cdot \tilde{\mathbf{S}}(0) \rangle_{\mathbf{h}=0} - \langle \tilde{\mathbf{S}}(0) \rangle_{\mathbf{h} \rightarrow \mathbf{0}}^2] \quad (4.1)$$

or

$$\chi = \frac{1}{2N} \lim_{\mathbf{p} \rightarrow \mathbf{0}} \langle \tilde{\mathbf{S}}(\mathbf{p})^* \cdot \tilde{\mathbf{S}}(\mathbf{p}) \rangle_{\mathbf{h}=0} \equiv \lim_{\mathbf{p} \rightarrow \mathbf{0}} \chi(\mathbf{p}), \quad (4.2)$$

where N is the number of lattice sites and $\tilde{\mathbf{S}}(\mathbf{p})$ is the Fourier transform of the spin fields $\mathbf{S}_i = (s_i, t_i)$:

$$\tilde{\mathbf{S}}(\mathbf{p}) \equiv \sum_{\mathbf{x}} \mathbf{S}(\mathbf{x}) e^{i\mathbf{p} \cdot \mathbf{x}}. \quad (4.3)$$

To measure the disordered-phase susceptibility in our simulations, we simply use the first term of (4.1).

For the ordered phase, the subtraction in (4.1) is delicate and we instead use (4.2), taking long, asymmetric lattices of size $L \times T \times T$ to get small values of the lowest non-zero momentum $p_{\min} = 2\pi/L$. In more detail, we find we can get good estimates of χ_- for fixed L by measuring $\chi(p)$ for the two lowest non-zero momenta in the long direction, $2\pi/L$ and $4\pi/L$, and then extracting χ_- by fitting to the form

$$\chi_-(p) \simeq \frac{1}{\chi_-^{-1} + c p^2}. \quad (4.4)$$

These estimates for χ_- converge fairly quickly as L is increased. Typical examples of such dependence are shown in fig. 12 for $x=0.5$ and 0.3. For the sake of using all our data, our final results for χ_- in table III are the result of a fit of these results for individual L to the form⁵ $a + bL^{-4}$. There is not too much difference between this and the individual result for the largest L . A list of the largest lattice size we use for each x may be found in table IV.

⁵ From (4.4), the difference between $\chi_-(p_{\min})$ and the true susceptibility χ_- scales as $p_{\min}^2 \sim L^{-2}$ for large L . Interpolating $\chi(p)$ from the two lowest non-zero momenta improves the error to L^{-4} . This is the reason for the form of our fit of these interpolated values vs. L .

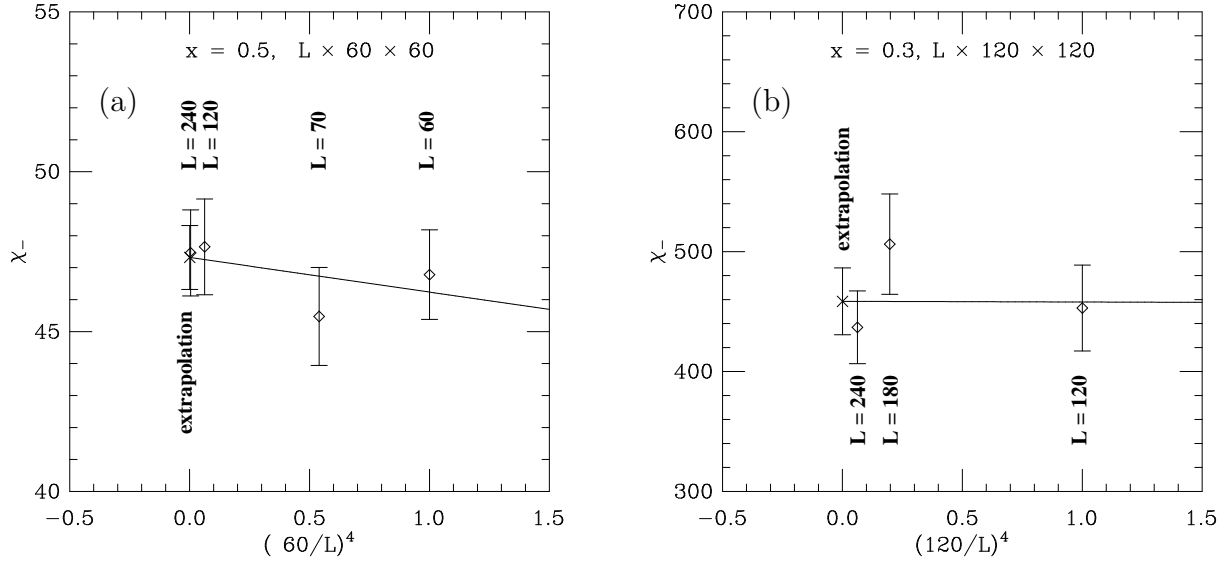


FIG. 12. Measurements of χ_- on $L \times T \times T$ lattices, using the interpolation (4.2), vs. L . The solid line is the best fit of the results to $a + bL^{-4}$, and the cross (and smaller error bar) at $L = \infty$ shows the extrapolation from this fit. Two cases typical of our data are shown: (a) $x=0.5$, $T=60$, with 63% confidence level; (b) $x=0.3$, $T=120$, with 18% confidence level.

B. Correlation Lengths

To measure correlation lengths, we first measure the correlation function

$$G(r) = \langle \mathbf{S}(0) \cdot \mathbf{S}(\mathbf{r}) \rangle, \quad (4.5)$$

where, in practice, we average the right-hand side over all translations and cubic rotations. We measure this correlation for the two cases of (1) displacements \mathbf{r} that lie along edges of the lattice (*i.e.* in the direction of nearest neighbors), and (2) those that lie along diagonals of the lattice. In each case, we also measure the full statistical error matrix of our measurements, which includes correlated errors between different r . (See sec. IV E for our method of computing statistical errors.) Then we fit $G(r)$ to the form

$$G(r) = a_+ \left[\frac{1}{r} e^{-r/\xi_+} + (\text{images}) \right] \quad (4.6)$$

for the disordered phase and

$$G(r) = a_- \left[\frac{1}{r} e^{-r/\xi_-} + (\text{images}) \right] + b_- \quad (4.7)$$

for the ordered phase. “Images” denotes the similar exponential contributions from nearby images of \mathbf{r} due to the finite periodicity of the lattice. We first try fitting the above forms to all the data points in the relevant direction (edge or diagonal). Then we iteratively throw away the smallest r point from our data set until both (1) the confidence level of the fit is at least 10%, and (2) $r > \xi$ for all the points being fit. Fig. 13 shows examples of fits to the correlation function.

Fig. 14 shows the effect of continuing to throw out even more and more short-distance points once our criteria are satisfied. Focusing on the fit to ξ_-^{edge} , there is a clear drift of ξ as more points are removed, and then there is a plateau that is high compared to our nominal value of ξ and its error (the left-most data point). One suspects that the value of ξ at this plateau might be a better estimate than that from our procedure. Unfortunately, we do not have a single, universal criterion that would exactly agree with one’s best subjective guess of ξ for every data set. The drift in values suggests that the systematic errors from fitting

may be a bit larger than the (statistical) errors we have assigned to ξ . If one strengthened the requirement $r > \xi$ for points being fit to $r > 1.5\xi$, this drift would change our final interpolations for the $x \rightarrow 0^+$ values of ξ_+/ξ_- from (3.17) to

$$\lim_{x \rightarrow 0^+} \frac{\xi_+^{\text{edge}}}{\xi_-^{\text{edge}}} = 1.55(5), \quad \lim_{x \rightarrow 0^+} \frac{\xi_+^{\text{diag}}}{\xi_-^{\text{diag}}} = 1.58(6), \quad (4.8a)$$

for extrapolation vs. $\xi_+^{-\omega}$ and

$$\lim_{x \rightarrow 0^+} \frac{\xi_+^{\text{edge}}}{\xi_-^{\text{edge}}} = 1.60(6), \quad \lim_{x \rightarrow 0^+} \frac{\xi_+^{\text{diag}}}{\xi_-^{\text{diag}}} = 1.64(9), \quad (4.8b)$$

for extrapolation vs. $\xi_-^{-\omega}$. This is comparable to the spread of values (3.17) and consistent with our final result (1.5).

The analysis of the correlation lengths for $x=0.3$ is slightly complicated. Because of the large lattice volume required, it takes longer to generate independent configurations than for other x . At the same time, we can measure the correlation function $G(r)$ at a larger number $N_r = 60$ of values of r . If the number of independent configurations is large compared to N_r , one can estimate the full covariance matrix (see sec. IV E) for all of these measurements and use it to find the correlation length. In our simulations, however, the number of independent configurations n generated for $x = 0.3$ (roughly 70 for the correlation function) is too small for this.⁶ We have chosen to circumvent this issue by simply throwing away many of our r values when fitting the correlation function, as we shall describe below. As we shall see, the $x = 0.3$ results do not much affect our final results for ξ_+/ξ_- ; so it is not necessary to make a more sophisticated analysis.

Fig. 15 shows the correlation function along diagonals for $x = 0.3$ at the transition in the ordered phase. Two regions of r plausibly contain the most important information for fitting the correlation function: the points at the largest r , which determine b_- in (4.7), and the points from one to a few correlation lengths, which determine ξ_- . We have chosen to keep only the r values marked by diamonds in fig. 15: every other point for 6 points at the largest

⁶ When $n \leq N_r$, for example, the measured covariance matrix will always be singular.

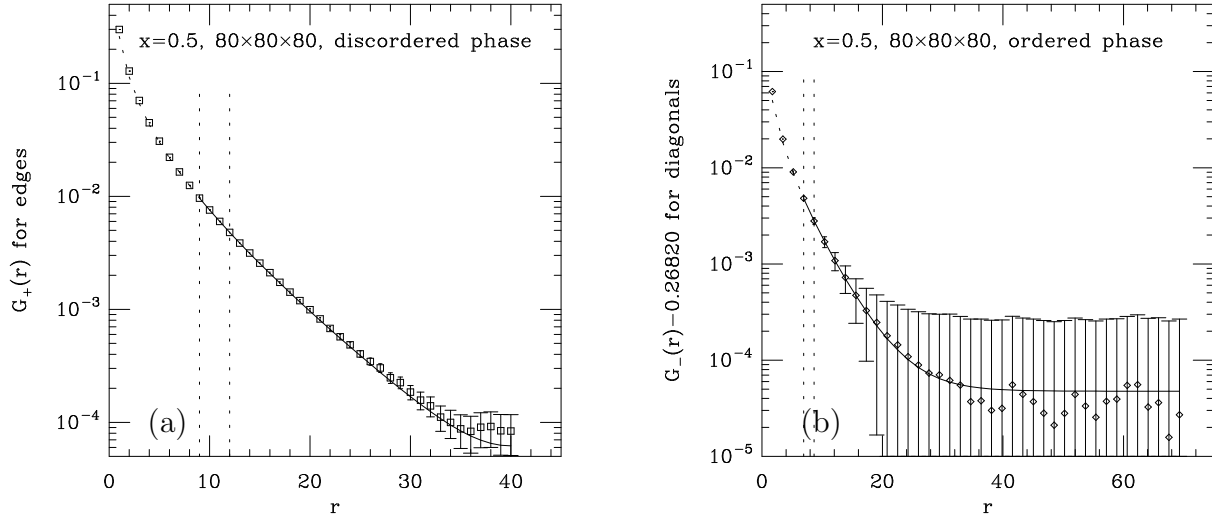


FIG. 13. Examples of fits to the correlation function $G(r)$ in (a) the disordered and (b) ordered phase. The scatter of points around the fits is small because of correlations between the points. The dotted vertical lines indicate the first point used with the criteria $r > \xi$ (left line, and the value used for the fit) or $r > 1.5\xi$ (right line).

r , and every other point for 7 points starting from $r \approx \xi$. We then have roughly five times as many independent measurements as r points. We use essentially the same prescription for the disordered phase and for the ξ_{\pm}^{edge} .⁷ The results previously quoted in sec. III were obtained using this method.

We have checked the sensitivity of our results to the choice of which points to keep. If we instead simply take 12 to 13 evenly spaced points between $r = \xi$ and r_{max} , we obtain $\xi_{+}/\xi_{-} = 1.42(7)$ for edges and $1.43(8)$ for diagonals at $x = 0.3$, as compared to $1.45(7)$ and $1.41(8)$ listed in table II. Due to the large error in our $x=0.3$ results, this change of prescription has negligible effect on the extrapolated ratios of ξ_{+}/ξ_{-} .

⁷ Actually, our somewhat arbitrary criteria was to always keep n/N_r as close as possible to 5. As a result, in some cases we took only 6 instead of 7 points starting from $r \approx \xi$.

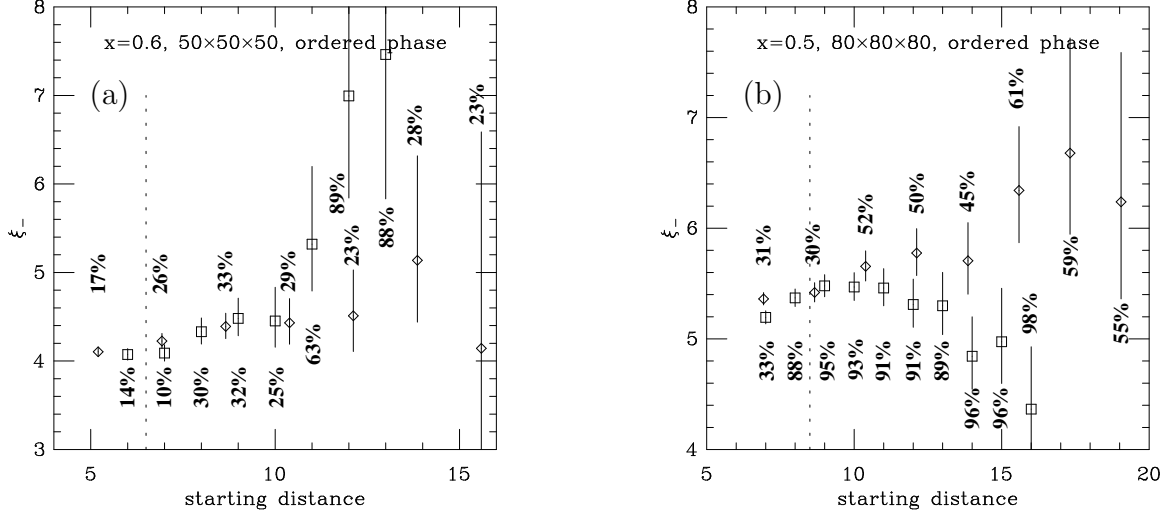


FIG. 14. Examples of the dependence of our fits for ξ on the minimum r kept in the fit. We show ξ_- for particular runs at β_t for (a) $x=0.6$ and (b) $x=0.5$. ξ_- is measured both along edges (squares) and diagonals (diamonds). The left-most point of each type is the point chosen for our final value, as described in the text. (The left-most point right of the dotted line is chosen if the criteria $r > 1.5\xi$ is used instead of $r > \xi$.) Confidence levels of the fit are given for each point.

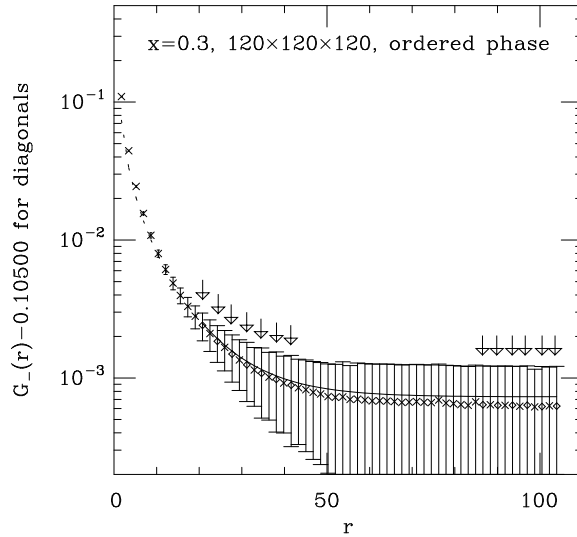


FIG. 15. Correlation function $G(r)$ along diagonals for $x = 0.3$ in the ordered phase at the transition. The diamonds represent the points actually used for the fitting and are also marked by arrows.

C. Finite volume effects

Table IV shows the largest lattice sizes we have used in the determination of various quantities. For all measurements, every lattice dimension is at least five times the correlation length and is typically ten times the correlation length. We shall assess whether finite volume errors are significant compared to our statistical errors. Finite size effects should generally fall exponentially with increasing lattice size.

x	$C_{\pm}, \xi_{\pm}, \chi_{+}$	χ_{-}	β_t	conversion
1.0	40^3	160×40^2	160×40^2	$40 \simeq 13.9 \xi_{+}^{\text{edge}}$
0.8	”	”	”	$40 \simeq 11.0 \xi_{+}^{\text{edge}}$
0.6	50^3	200×50^2	”	$50 \simeq 9.4 \xi_{+}^{\text{edge}}$
0.5	80^3	240×60^2	240×60^2	$80 \simeq 11.0 \xi_{+}^{\text{edge}}$
0.3	120^3	240×120^2	480×120^2	$120 \simeq 5.4 \xi_{+}^{\text{edge}}$

TABLE IV. Largest volumes used for various measurements. The last column gives a conversion between a typical lattice dimension and the disordered phase correlation length ξ_{+}^{edge} (which is larger than ξ_{-}).

In many Monte Carlo applications, the cleanest way to show that finite volume effects are negligible for a given lattice volume is to repeat the simulation on smaller and smaller volumes until the effects are clearly noticeable. One then extrapolates the finite size corrections back to the original, large volume. Unfortunately, this procedure is problematical in our case. In smaller volumes, the system undergoes transitions between the ordered and disordered phases. One can still measure quantities such as C_{\pm} during a time period between transitions, but, as the volume and that transition time decreases, the statistical error of the measurement will increase. This degradation of the statistics for smaller volumes obscures the finite size effects one would like to measure.

Instead, we content ourselves with simulating the system for a few different “large” volumes and checking whether the discrepancies seem consistent with statistical error. Fig. 16 shows our checks. The data for C_{+}/C_{-} and ξ_{+}/ξ_{-} look pretty good. The data for χ_{+}/χ_{-}

suggests there might be a systematic effect making our larger volume measurements slightly larger than our lower volume measurements. In any case, we estimate that our finite size errors are no larger than our statistical errors.

We do not have data for $x=0.3$ but, based on the sizes of the correlation lengths, $x=0.3$ on our 120^3 lattice should be roughly comparable to $x=0.6$ on a 30^3 lattice. A portion of a run on the latter is shown in fig. 17. Not only do we see a transition between the phases, but we also see a small spike corresponding to an aborted transition attempt. Whether or not such spikes appear in one's data can have a significant effect on the extraction of the specific heat. For instance, if the run shown were cut off just before the spike, one would find $C_+ = 2.36(4)$. If the run were cut-off just after the spike, one would find $C_+ = 2.51(10)$ and suddenly have drastically revised the error estimate. It is because of this sort of finite-size effect that we distinguish our $x = 0.3$ data as slightly less reliable.

In a few cases, we have checked the possibility of finite size errors in our determination of β_t . (Determining β_t is quite time consuming.) Table V shows the results for different choices of the transverse size T of the $L \times T \times T$ lattices we use for determining the transition temperature. The values are consistent with each other and, based on the transverse sizes of our lattices in units of ξ_+ (as given by table IV), we believe that our measurements for other x should be reliable as well.

x	lattices	β_t
1.0	$L \times 20^2$	0.157156(12)
	$L \times 40^2$	0.157154(4)
0.5	$L \times 40^2$	0.186750(4)
	$L \times 60^2$	0.186751(3)
0.3	$L \times 80^2$	0.200362(3)
	$L \times 120^2$	0.2003659(15)

TABLE V. Dependence of the determination of β_t on transverse lattice size for those x where we measured it.

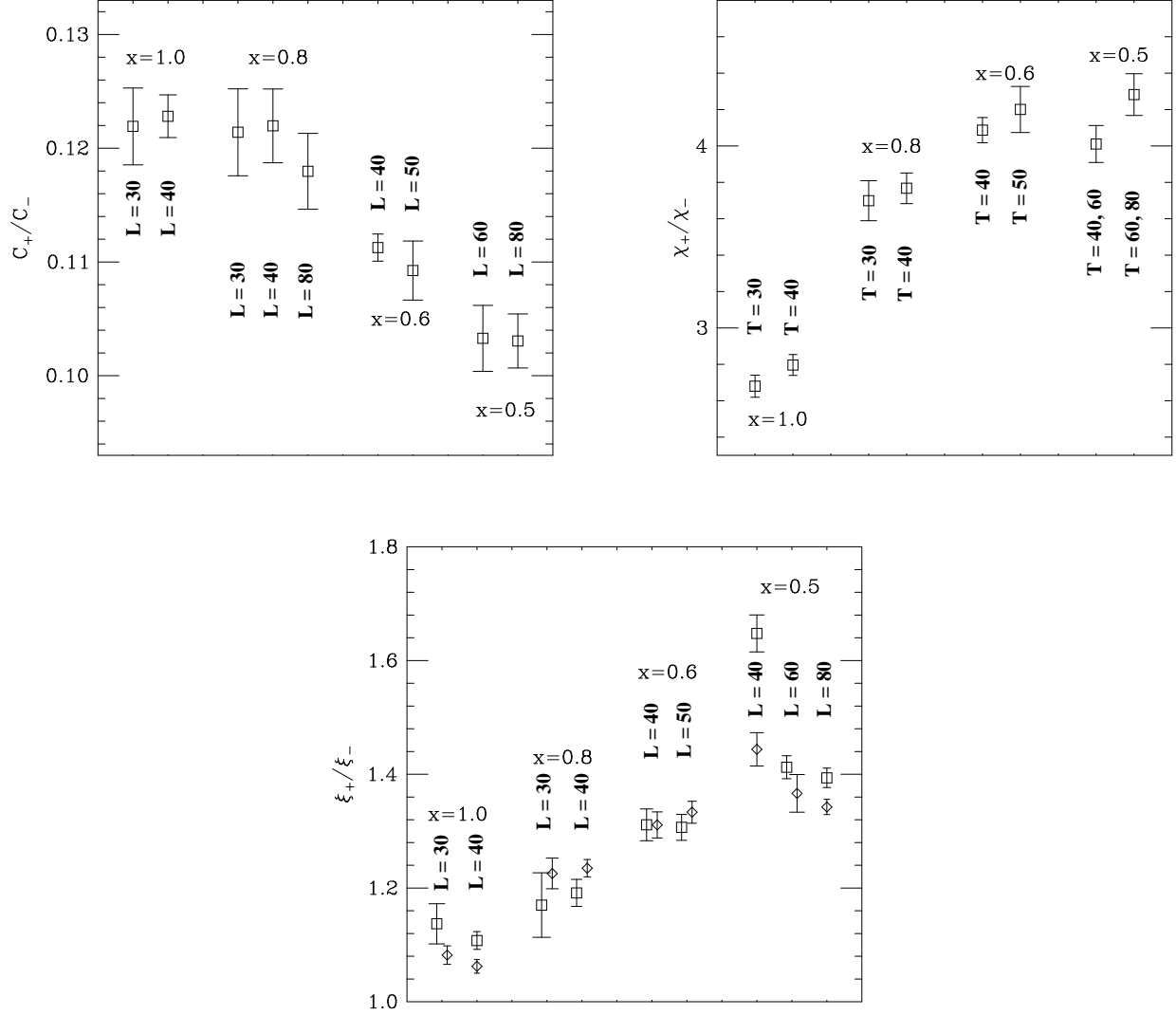


FIG. 16. Checks of volume dependence of our ratios for all of our values of x . C_{\pm} and ξ_{\pm} were measured on an L^3 lattice. χ_+ was measured on a T^3 lattice, and χ_- was extrapolated on $L \times T^2$ lattices. Where there are two values of T specified, the first is for χ_- and the second for χ_+ . For the ξ ratio, the squares and diamonds are the results along edges and diagonals respectively. Error bars do not include the uncertainty in β_t .

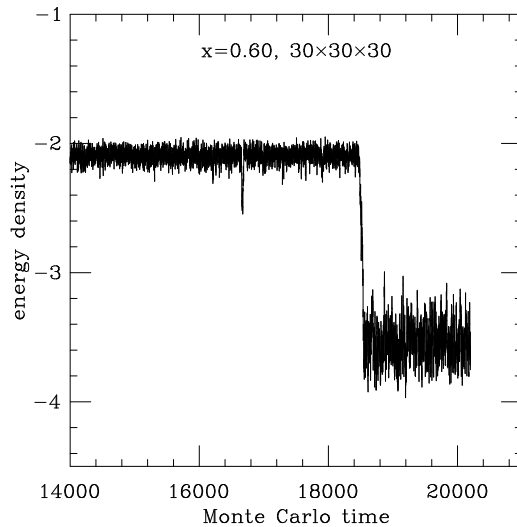


FIG. 17. The internal energy vs. Monte Carlo time for an $x=0.6$ run on a somewhat smallish lattice (30^3). This section of the run shows a transition between the phases and, preceding it, a spike corresponding to an unsuccessful transition attempt.

D. Transition temperature uncertainties

1. Determining β_t

As discussed in the introduction, our procedure for determining the transition temperature is to make multiple runs starting from mixed-phase initial conditions on long, asymmetric lattices ($L \times T \times T$) and to find the β for which the system is equally likely to end up in the ordered or disordered phase. A simple, biased random walk model of this process is presented in appendix B, which predicts that the probability P of ending up in the ordered rather than disordered phase should have β dependence of the form:

$$P \simeq \frac{1}{2} \left[1 + \tanh \left(\frac{\beta - \beta_t}{\Delta\beta} \right) \right], \quad (4.9)$$

where β_t and $\Delta\beta$ are not determined by the model and $\Delta\beta$ may depend on the transverse lattice size and on the Monte Carlo algorithm. An example of our data, and the tanh curve that best fits it, is shown in fig. 18.

At the beginning of each simulation, we obtain the initial condition of fig. 3 by initializing one half of the lattice with $\beta=0$ initial conditions, one half with $\beta=\infty$ initial conditions, and

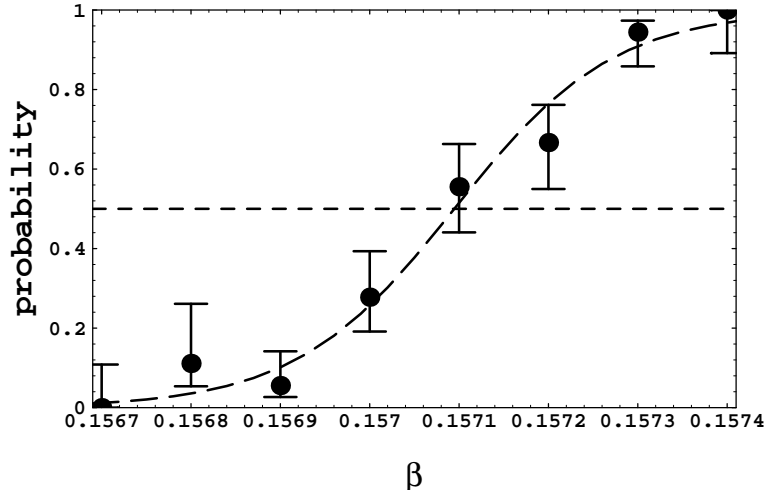


FIG. 18. An example of the probability of ending in the ordered phase vs. β when starting with mixed initial conditions. The data is for $x = 1.0$ (the 4-state Potts model) on a 40×20^2 lattice. The fit (dashed line) to (4.9) has a 75% confidence level. (This is typical of our fits to other data, at smaller x or different lattice spacings, where the confidence levels of samples we checked ranged randomly from roughly 45% to 85%. At smaller x , we generally have somewhat fewer measurements and hence somewhat larger statistical uncertainty than shown above.)

then evolving the two halves independently for roughly 1000 sweeps (depending on x) at the desired β . Only then are the two halves allowed to interact and the interface allowed to move, and the entire system is then evolved together.

Appendix B also discusses why the β_t determined by fitting (4.9) is not necessarily correct for finite L , and the model predicts the correction to the true β_t scales like $1/L^2$. We therefore fit β_t for a variety of L and have extrapolated to get the final values of table III. An example is shown in fig. 19. Data is shown for two different transverse lattice sizes, which have different $1/L^2$ corrections but extrapolate to consistent $L \rightarrow \infty$ limits.

The simple model of Appendix B also predicts that the width $\Delta\beta$ of the tanh curves should scale like $1/L$. Though this is not directly relevant to our determination of β_t , it is worth checking. Fig. 20 shows a fit of this behavior to the data corresponding to fig. 19. The fit is not very good for the $L \times 40^2$ data, with 2% confidence level, and this mediocrity is typical of our data at other values of x . In contrast, our fits for β_t typically work fairly well. We suspect that the failure of our model for $\Delta\beta$ may be due to the non-local nature of the cluster algorithm.

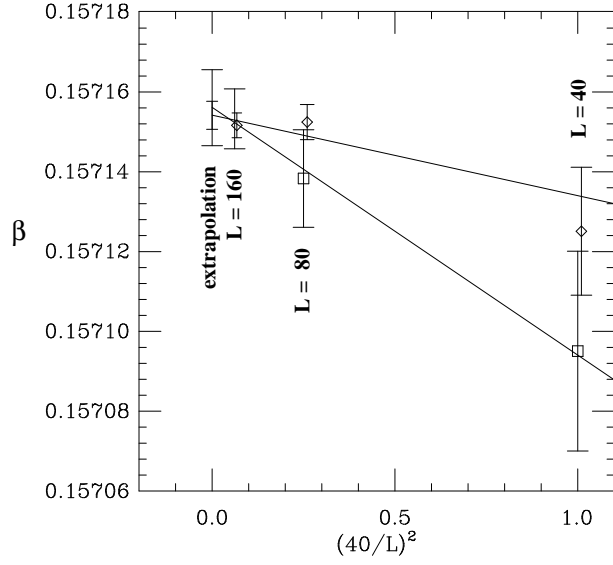


FIG. 19. An example of the finite L dependence of our determination of β_t . The data is for $x=1.0$ on (squares) $L \times 20^2$ and (diamonds) $L \times 40^2$ lattices. (For $L=160$, the smaller error bar is the diamond point.) The lines are the best fits to the form $a + bL^{-2}$, and the extrapolations (see table V) are shown at $L=\infty$.

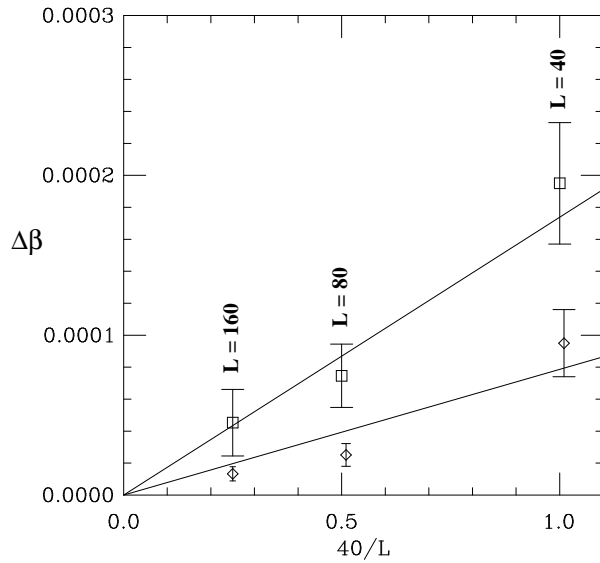


FIG. 20. An example of the finite L dependence of the width $\Delta\beta$ of our fits to tanh curves. The data is for the same simulations as in fig. 19. The lines are the best fits to a/L .

2. Effects on other measurements

Given our estimates of the uncertainty in the transition temperature (see Table III), we now need to determine the resulting uncertainties in our measurements of C , ξ , and χ . For C and χ , we do this by measuring

$$\partial_\beta(\beta^{-2}C) = -N^2\langle(\epsilon - \bar{\epsilon})^3\rangle, \quad (4.10)$$

$$\partial_\beta\chi = -N[\langle\chi\epsilon\rangle - \langle\chi\rangle\langle\epsilon\rangle], \quad (4.11)$$

where N is the lattice volume, $\epsilon = E/N$ is the energy density, and $\bar{\epsilon} \equiv \langle\epsilon\rangle$. We make our measurements at the central value of β_t . Results are given in table VI. Our determination of these derivatives at small x is not particularly good, but it only needs to be good enough to estimate our error due to the uncertainty in β_t . For the correlation length, we similarly compute the β derivatives of the correlation function and of our error matrix. The separate sizes of statistical errors and β_t uncertainty errors in our final results is given in table VII.

x	$\partial_\beta(\beta^{-2}C_+)$	$\partial_\beta(\beta^{-2}C_-)$	$\partial_\beta\chi_+$	$\partial_\beta\chi_-$
1	$2.14(17)\times 10^4$	$-4.0(6)\times 10^5$	$1.29(6)\times 10^4$	$-1.39(20)\times 10^4$
0.8	$2.2(3)\times 10^4$	$-6.5(1.2)\times 10^5$	$2.55(18)\times 10^4$	$-1.82(17)\times 10^4$
0.6	$4.0(5)\times 10^4$	$-9.4(1.9)\times 10^5$	$8.7(9)\times 10^4$	$-6.2(5)\times 10^4$
0.5	$6.7(8)\times 10^4$	$-1.5(4)\times 10^6$	$2.42(19)\times 10^5$	$-1.99(22)\times 10^5$
0.3	$4.9(1.2)\times 10^5$	$-2.3(1.0)\times 10^7$	$1.30(24)\times 10^7$	$-1.21(23)\times 10^7$

TABLE VI. Summary of β derivatives of C_\pm and χ_\pm at the central value of β_t .

x	$\delta\beta_t$ error / stat. error			
	C_+/C_-	ξ_+/ξ_-	χ_+/χ_-	edge diag.
1	0.2	0.2	0.3	0.3
0.8	0.2	0.1	0.2	0.2
0.6	0.2	0.3	0.3	0.3
0.5	0.5	0.7	0.8	0.8
0.3	0.4	0.5	0.4	0.4

TABLE VII. Relative size of error due to uncertainty in β_t compared to the statistical error for the ratios whose total errors are given in table II. The total error is the β_t uncertainty added in quadrature with the statistical errors. (For χ_- , “statistical error” includes the extrapolation $L \rightarrow \infty$.)

E. Statistical errors and algorithms

Statistical errors were determined by first computing the decorrelation time τ_d relevant for each quantity. (For example, for C , we use the decorrelation time in the energy.) By decorrelation time, we mean a measure of the Monte Carlo time over which configurations *within a given phase* become statistically uncorrelated. Our decorrelation time does not measure the mixing time between phases, since we run in large enough volumes that there are no transitions between phases in our simulations.

Consider first estimating the error of quantities which are determined by simple ensemble averages of some quantity A (e.g. the susceptibilities $\chi(p)$ or the energy density ϵ). We then use the integrated decorrelation time defined by [16]

$$\tau_{int} = \frac{1}{2} \sum_{t=-\infty}^{+\infty} C(A; t). \quad (4.12)$$

$C(A; t)$ is the auto-correlation function, estimated for a sample of n measurements as [17]

$$C(A; t) = \frac{\frac{1}{n-t} \sum_{i=1}^{n-t} (A_i - \bar{A})(A_{i+t} - \bar{A})}{\sigma_A^2}, \quad (4.13)$$

where \bar{A} is the sample average of A and

$$\sigma_A^2 = \frac{1}{n} \sum_{i=1}^n (A_i - \bar{A})^2. \quad (4.14)$$

The error in \bar{A} is then estimated as

$$\text{Err}(\bar{A}) = \sigma_A \sqrt{\frac{2\tau_{int}}{n}} \quad (4.15)$$

In practice, the sum in the definition (4.12) must be cut off, because the statistical error in $C(A;t)$ itself becomes large for large t . Our criteria is to cut off the sum when $C(A;t)$ drops below 0.05. The value 0.05 was chosen to give reasonable agreement with the binning method described next. Reducing 0.05 to 0.01 would not appreciably change our results.

Alternatively, one can estimate errors by binning the sequence of measurements A_i ($i = 1, n$) into bins of some size τ_{bin} and averaging the data over each bin to obtain a new sequence \bar{A}_k ($k = 1, N_{bin}$), where $N_{bin} = n/\tau_{bin}$. The error is then estimated by the variance of this new sequence:

$$[\text{Err}(\bar{A})]^2 = \frac{1}{(N_{bin} - 1)} [\langle \bar{A}^2 \rangle - \langle \bar{A} \rangle^2]. \quad (4.16)$$

Fig. 21 shows a typical example of the result vs. bin size. The error stabilizes at large bin sizes, as it should, and roughly agrees with the integrated decorrelation time method, which is also shown in the figure.

To calculate correlation lengths, we need the full correlated error matrix (the covariance matrix) of the correlation functions $G(r)$. We compute this using the binning method. Binning (with fixed bin size) has the advantage that the resulting covariance matrix is positive definite. The covariance matrix is given by

$$\sigma_{ij} = \frac{1}{(N_{bin} - 1)} [\langle \bar{\mathcal{G}}(r_i) \bar{\mathcal{G}}(r_j) \rangle - \langle \bar{\mathcal{G}}(r_i) \rangle \langle \bar{\mathcal{G}}(r_j) \rangle], \quad (4.17)$$

where $\mathcal{G}(r) = \mathbf{S}(\mathbf{r}) \cdot \mathbf{S}(0)$ averaged over translations and cubic rotations. In order to have a simple universal criteria for what size of bin to use, we have surveyed a variety of examples and found that a bin size of $10\tau_d$ works well, where τ_d is the maximum (over the range of r

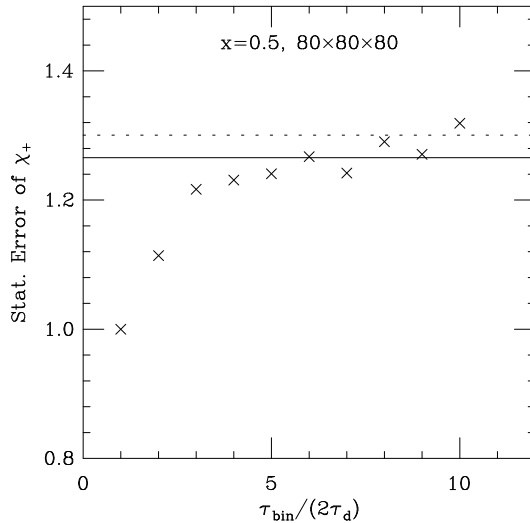


FIG. 21. Example of statistical error estimates vs. bin size. The data is from measurements of χ_+ at $x = 0.5$. The vertical axis has been arbitrarily normalized to be 1.0 for $\tau_{\text{bin}} = 2\tau_d$. The solid horizontal line is the independent error estimate using the integrated decorrelation time. The dotted line is what the same estimate would be if we had cut off the sum (4.12) when $C(A; t)$ dropped below 0.01 rather than 0.05.

used for the fit) of the integrated decorrelation time for the $G(r)$. Fig. 22a shows a typical example of the dependence of the statistical error of correlation length on bin size, and our particular choice of bin size can be seen to be adequately large.

The error estimate for the correlation lengths are determined by a standard chi-square analysis.

One case that requires a slightly different approach is the specific heat, which is measured from the variance of the energy density. In this case, we bin the energy density as above but don't average it over each bin. Then we apply the jackknife procedure on the bins: we compute the specific heat after throwing away the τ_{bin} energy density measurements corresponding to one of the bins. The N_{bin} possibilities for which bin to have thrown out gives us N_{bin} separate measurements of the specific heat. The variance of these measurements is used for the error estimate on the specific heat. By surveying the dependence on bin size for all our data, we have found that a good choice is $\tau_{\text{bin}} = 10\tau_d$ where τ_d is the integrated decorrelation time for the energy. An example of the dependence on bin size is shown in Fig. 22b.

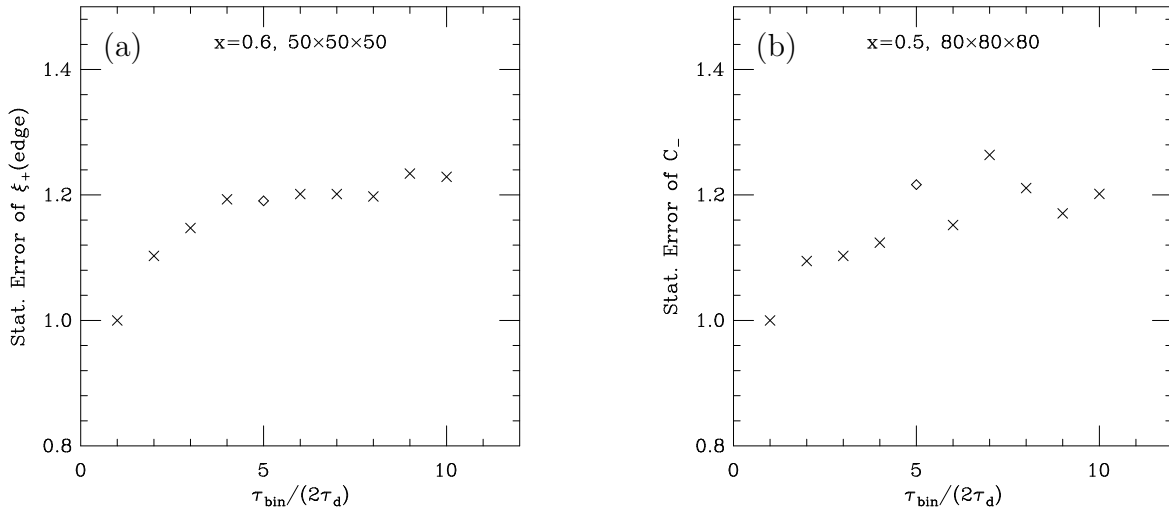


FIG. 22. Examples of the dependence of statistical error on bin size for (a) ξ_+^{edge} , and (b) C_- . The vertical axis has been arbitrarily normalized to be 1.0 for $\tau_{\text{bin}} = 2\tau_d$. The diamond marks the actual bin size used according to our criteria.

A similar approach is used for χ_- and all β derivatives (*e.g.* $\partial_\beta \chi_\pm$).

We have checked that running simulations with a pure heatbath algorithm, or with a pure cluster update algorithm, give results that are statistically consistent with each other and with our interlacing of the two algorithms.⁸

This work was supported by the U.S. Department of Energy, grants DE-FG06-91ER40614 and DE-FG03-96ER40956. We thank Joseph Rudnick, Michael Fisher, Joan Adler, and David Wright for useful conversations, Peter Ungar for explaining the solution to the Gambler's Ruin problem, Marcel Den Nijs for pointing out that the cross-over exponents are

⁸ In fact, such checks led us to discover for ourselves the problems of naively using simple random-number generators. We had initially used a 32-bit congruence algorithm with a period of 2^{32} . This period is too small for the length of some of our simulations, manifesting in inconsistency between the heatbath and cluster algorithms and producing correlations which could clearly be seen in the very-long-time tail of the energy auto-correlation function. We had to switch to a generator with period 2^{64} .

determined by well-known Ising model critical exponents, and, most of all, Steve Sharpe and Larry Yaffe, who gave too many valuable suggestions to enumerate.

APPENDIX A: CLUSTER UPDATE ALGORITHM

The two of us have used different versions of a cluster update algorithm, one which grows and flips a single cluster at a time, and another which grows simultaneous clusters across the entire lattice. In any case, they are simple generalizations of the algorithms [18,13] used in other spin systems. Write the Hamiltonian as

$$\beta H = \sum_{\langle ij \rangle} h(\mathbf{S}_i, \mathbf{S}_j) \quad (\text{A1})$$

where $h(\mathbf{S}_i, \mathbf{S}_j)$ is the nearest-neighbor interaction.

One step of the first version of the algorithm can be summarized as follows. (a) Randomly choose one of the five order-2 elements R ($R^2 = 1$) of the internal symmetry group D_4 . (b) Randomly choose a lattice site x as the first point to include in the cluster c , and mark the site. (c) One at a time, visit all new links $\langle xy \rangle$ connecting $x \in c$ to its nearest neighbors y . For each link visited, check if y is already in c , and if not then adjoin it to c with probability $P(\mathbf{S}_x, \mathbf{S}_y)$, where

$$P(\mathbf{S}_x, \mathbf{S}_y) = 1 - \exp \{ \min[0, h(\mathbf{S}_x, \mathbf{S}_y) - h(R\mathbf{S}_x, \mathbf{S}_y)] \} . \quad (\text{A2})$$

A newly included y should be marked. (d) Repeat step (c) until no new sites are added to the cluster. (e) Flip all the spins in the resulting cluster: $\mathbf{S} \rightarrow R\mathbf{S}$.

Randomness of the choices in steps (a) and (b) is inessential: one only needs to vary the choices enough to give reasonably efficient ergodicity. If (a) is restricted to a random choice between just the two symmetries corresponding to $s \rightarrow -s$ and $t \rightarrow -t$ respectively, then this algorithm is equivalent to the Ashkin-Teller cluster algorithm described in ref. [19]. (See also ref. [20].)

One step of the second version of the algorithm is as follows. (a) Randomly choose an R as above. (b) Visit every link $\langle xy \rangle$ in the lattice and mark it with probability $P(\mathbf{S}_x, \mathbf{S}_y)$

given by (A2). (c) Identify all the disconnected clusters of sites connected by marked links, and flip each such cluster with probability $1/2$.

APPENDIX B: THE GAMBLER'S RUIN PROBLEM

In section II, we discussed how we determine the transition temperature by splitting an asymmetric $L \times T \times T$ lattice in half along the longitudinal direction L and starting the two halves in the ordered and disordered phases respectively. In this appendix, we explain a simple model for the probability of the system evolving into one phase over the other.

At any time, let z_1 and z_2 be the (transversely averaged) locations of the two domain walls, and let z be the separation between them as measured through the disordered phase (or $L - z$ as measured through the ordered phase). When $\beta = \beta_t$, z should random walk in Monte Carlo time. When β deviates slightly from β_t , there will be a slight bias in this random walk proportional to $\beta - \beta_t$. If we model this biased random walk as taking fixed steps in z with probability

$$\text{prob}(z \rightarrow z+1) \equiv p = \frac{1}{2}(1 + \epsilon), \quad (\text{B1})$$

$$\text{prob}(z \rightarrow z-1) \equiv q = \frac{1}{2}(1 - \epsilon), \quad (\text{B2})$$

where $\epsilon \propto \beta - \beta_t$ is small, then we have a special case of the Gambler's Ruin problem. The Gambler's Ruin problem is that you start with z dollars in your pocket and you play some casino game over and over again until you either go broke or accumulate your goal of L dollars. What is the probability you can afford the taxi home?

To solve it, let $P(z)$ be the probability of winning if you start at z . Then, by considering one step, one obtains the difference equation

$$P(z) = pP(z+1) + qP(z-1), \quad (\text{B3})$$

and the boundary conditions are

$$P(0) = 0, \quad P(L) = 1. \quad (\text{B4})$$

The solution is

$$P(z) = \frac{1 - \left(\frac{q}{p}\right)^z}{1 - \left(\frac{q}{p}\right)^L}. \quad (\text{B5})$$

In our case (small ϵ and large L), this becomes

$$P(z) \simeq \frac{1 - e^{-2\epsilon z}}{1 - e^{-2\epsilon L}}. \quad (\text{B6})$$

Putting in our initial condition $z = L/2$, we find that the curve in fig. 5a is a tanh curve:

$$P(L/2) \simeq \frac{1}{2}[1 + \tanh\left(\frac{1}{2}\epsilon L\right)]. \quad (\text{B7})$$

We don't know *a priori* the proportionality constant between our parameter ϵ and $\beta - \beta_t$, but we can parametrize the curve as

$$P \simeq \frac{1}{2} \left[1 + \tanh\left(\frac{\beta - \beta_t}{\Delta\beta}\right) \right] \quad (\text{B8})$$

and determine β_t and $\Delta\beta$ by fitting to our Monte Carlo results. We haven't attempted to model the dependence of ϵ on transverse size T . However, for fixed transverse size the model (B7) predicts

$$\Delta\beta \propto 1/L. \quad (\text{B9})$$

As mentioned in sec. II, there are systematic errors which make the center of the tanh curves shift as L is increased. One example would occur if the two halves aren't adequately equilibrated at the inverse temperature β before allowing the domain walls to evolve. Then, even exactly at β_t , there might be some systematic bias to the initial motion of the walls until thermal equilibrium is reached. This could be modeled by simply starting z with some systematic initial offset, *i.e.* $z = L/2 + a$. Secondly, even if proper equilibrium is reached, the "stickiness" of the domain walls need not be the same in the two phases. For example, we have only been discussing the average longitudinal coordinates z_1 and z_2 of the domain walls. In fact, the domain walls have transverse excitations and might have slightly longer, thinner fingers reaching out into one phase than into the other. The separation at which

they first touch each other might be larger in one phase than in the other. Such an effect could be modeled by considering the effective end-points of the game to be slightly and asymmetrically different from $z=0$ and $z=L$, now being $z=b_1$ and $z=L - b_2$. By a shift of coordinate, this can again be considered as the problem of starting slightly away from $z = L/2$.

So a model for the systematic error is to ask what happens if the probability is really $P(L/2 + a)$ from (B6), for some a , but we nonetheless tried to extract a value of β_t fitting the form $P(L/2)$ for (B7) to the result. One easily finds that the systematic error in β_t then scales as $1/L^2$ for large L (assuming fixed transverse dimension and hence a fixed proportionality between ϵ and $\beta - \beta_t$).

APPENDIX C: BCC LATTICES

We have made a few simulations on BCC lattices, but not enough to extract any $x \rightarrow 0$ limits. Our results are presented in table VIII. The measurements of C_{\pm} were made on 40^3 lattices; β_t was measured on lattices as big as 160×20^2 for $x=1.0$ and 80×40^2 for $x=0.6$. When we refer to an $L_1 \times L_2 \times L_3$ BCC lattice, we mean one with $L_1 L_2 L_3$ unit cells and so $N = 2L_1 L_2 L_3$ sites. All of our lattices are helical. Defining helical boundary conditions on a BCC lattice is perhaps non-standard, and we explain it below.

x	β_t	ϵ_+	C_+	C_+/C_-
		ϵ_-	C_-	
BCC:				
1	0.113752(5)	-2.344(4)	1.34(24)	0.112(3)
		-5.808(5)	11.9(3)	
0.6	0.130291(6)	-2.1975(8)	1.88(4)	0.104(4)
		-4.392(7)	18.1(5)	

TABLE VIII. Same as table III but for BCC lattices. Densities are given in units of per lattice point, which for BCC differs from per unit cell.

Helical boundary conditions for BCC lattices

To motivate our definition of helical boundary conditions for BCC lattices, we first briefly review the situation for simple cubic lattices and, for simplicity of presentation, will first consider two-dimensional examples. Fig. 23 shows an infinite simple cubic lattice in two dimensions. A finite-volume lattice with periodic boundary conditions corresponds to restricting the system to the sites inside a box, such as shown in fig. 23a, and then identifying opposite edges of the box. The same volume with helical boundary conditions corresponds instead to the box in fig. 23b, again with opposite edges identified. Helical boundary conditions retain translation invariance. Their advantage is that the sites can be numbered, as shown in fig. 23b, in such a way that the offset between one site and its neighbor in a given direction is always a fixed number modulo N , independent of the site chosen, where N is the total number of sites. For the two-dimensional lattice shown, the offsets Δn corresponding to the four directions are

$$\Delta n = \pm 1, \pm L_1 \text{ mod } N=L_1L_2. \quad (\text{C1})$$

In the three-dimensional case, they are

$$\Delta n = \pm 1, \pm L_1, \pm L_1L_2 \text{ mod } N=L_1L_2L_3. \quad (\text{C2})$$

The nature of these offsets is an advantage because, if the lattice is represented as a linear array in memory, it makes indexing neighbors of sites quicker and easier than for periodic lattices. (C2) is the definition used in this paper for an $L_1 \times L_2 \times L_3$ helical simple cubic lattice.

Fig. 24a shows a somewhat similar box drawn for a BCC lattice.⁹ Unfortunately, there

⁹ In two dimensions, an infinite BCC lattice is of course equivalent to a simple cubic lattice. We are discussing it just as a visual aid for generalizing to three-dimensional BCC lattices.

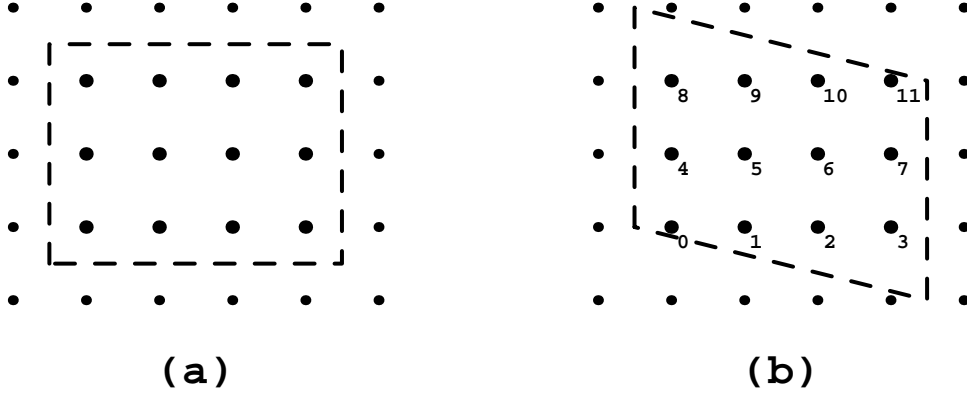


FIG. 23. Ways to choose a finite volume box from the infinite plane and impose periodicity corresponding to (a) normal periodic boundary conditions, and (b) helical boundary conditions.

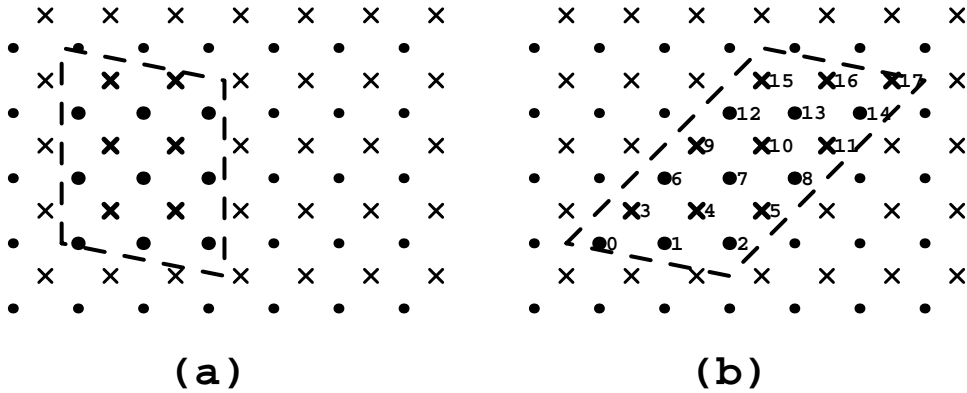


FIG. 24. Ways to try to choose a finite volume box for a BCC lattice. (a) lacks the advantages of the helical simple cubic case; (b) is our definition of a helical BCC lattice.

is no way to number the sites in the box so that the offset Δn between neighbors is the same for all sites. However, if one instead draws the box as in fig. 24b, such numberings are possible. For two-dimensions, the numbering of fig. 24b corresponds to

$$\Delta n = \pm L_1, \pm(L_1 - 1) \bmod N=2L_1L_2, \quad (\text{C3})$$

For three dimensions, where there are 8 nearest-neighbor directions, the generalization is

$$\Delta n = \pm L_1L_2, \pm(L_1L_2 - 1), \pm(L_1L_2 - L_1), \pm(L_1L_2 - L_1 - 1) \bmod N=2L_1L_2L_3. \quad (\text{C4})$$

This is our definition of an $L_1 \times L_2 \times L_3$ helical BCC lattice.

APPENDIX D: A MODEL OF RATIOS AND CROSS-OVER EXPONENTS FOR SMALL α

1. Overall scaling

In this appendix, we elaborate on the assertions of sec. III A about how small x needs to be if the Ising critical exponent α is formally considered small. We begin by reviewing the case of non-small α in slightly more detail. For the sake of specificity, we focus on the behavior of the correlation lengths ξ_{\pm} . The correlation functions $G_{\pm}(R) = \langle s(R)s(0) \rangle_{\pm}$ will have the following form of universal cross-over scaling function near the transition for small x :

$$G_{\pm}(R) = b^{-y} G_{\pm}(b^{y_t} t, b^{y_x} x, b^{-1} R), \quad (\text{D1})$$

where b is the arbitrary renormalization distance scale and

$$y = d - 2 + \eta, \quad y_t = 1/\nu, \quad y_x = \alpha/\nu \quad (\text{D2})$$

are the anomalous dimensions of G_{\pm} , t , and x . We have ignored the effects of irrelevant operators. t is a scaling field corresponding to the reduced temperature. In this language,

the derivation of the relationship between ξ_{\pm} and x can be made by first choosing $b = x^{-1/y_x}$ and writing

$$G_{\pm}(R) = x^{y/y_x} G_{\pm}(x^{-y_t/y_x} t, 1, x^{1/y_x} R). \quad (\text{D3})$$

As we vary t , the transition must occur for some definite value τ_0 of the first-argument on the left-hand side:

$$G_{\pm}(R) = x^{y/y_x} G_{\pm}(\tau_0, 1, x^{1/y_x} R). \quad (\text{D4})$$

By dimensional analysis, the long-distance behavior of the right-hand side of (D4) must have the form

$$G_{\pm}(\tau_0, 1, r) \sim e^{-r/A_{\pm}}, \quad (\text{D5})$$

and so

$$\xi_{\pm} \sim A_{\pm} x^{-1/y_x}, \quad (\text{D6a})$$

$$\frac{\xi_+}{\xi_-} \sim \frac{A_+}{A_-} \sim x^0. \quad (\text{D6b})$$

Now we can discuss the case where α is small or zero. (D1) was a special case of a more general situation where x doesn't scale as a power law. To be more general, replace

$$b^{y_x} x \rightarrow \bar{x}(b), \quad (\text{D7})$$

where $\bar{x}(b)$ is the solution to some renormalization-group equation. The non-small α case corresponded to

$$b \partial_b \bar{x} = y_x \bar{x} + O(\bar{x}^2) = \frac{\alpha}{\nu} \bar{x} + O(\bar{x}^2), \quad (\text{D8})$$

The form (D1) corresponds to ignoring the $O(\bar{x}^2)$ correction for small x , giving a simple, power-law solution for \bar{x} . When $\alpha = 0$, on the other hand, the $O(\bar{x}^2)$ terms in (D1) become essential:

$$b \partial_b \bar{x} = c \bar{x}^2 + O(\bar{x}^3), \quad (\text{D9})$$

where we assume $c > 0$. ($c \leq 0$ would lead to a second-order Ising phase transition for small $x > 0$ and so is excluded if we assume the phase transition remains first-order.) Ignoring the $O(\bar{x}^3)$ terms, this corresponds to our original scaling function (D1) with

$$b^{yx} x \rightarrow \frac{1}{x^{-1} - c \ln b}. \quad (\text{D10})$$

For very small x , we now want to choose

$$b \sim e^{1/cx}, \quad (\text{D11})$$

which gives $\xi_{\pm} \sim e^{1/cx}$ as discussed in sec. III A. However, just as in (D6b), one will still get

$$\frac{\xi_+}{\xi_-} \sim \frac{A_+}{A_-} \sim x^0. \quad (\text{D12})$$

Now we're ready to model the case where α is arbitrarily small but non-zero. Clearly we do not want to ignore the $O(\bar{x}^2)$ term in the renormalization group equation, so we take

$$b \partial_b \bar{x} = \frac{\alpha}{\nu} \bar{x} + c \bar{x}^2 + O(\bar{x}^3). \quad (\text{D13})$$

Ignoring higher-order terms, the solution is

$$\bar{x}(b) = \frac{b^{\alpha/\nu} x}{1 - (b^{\alpha/\nu} - 1) \frac{\nu c x}{\alpha}}, \quad (\text{D14})$$

which gives

$$\xi_{\pm} \sim \left(\frac{1 + \frac{\alpha}{\nu c x}}{1 + \frac{\alpha}{\nu c}} \right)^{\nu/\alpha}, \quad (\text{D15})$$

which interpolates between the previous cases and has the properties summarized in sec. III A. But, just as in the previous cases, again

$$\frac{\xi_+}{\xi_-} = \frac{A_+}{A_-} \sim x^0. \quad (\text{D16})$$

So the ratio is insensitive to the crossover between exponential and power-law dependence of ξ_{\pm} on x^{-1} .

2. Corrections to scaling

To address corrections to scaling, supplement (D1) by the most important irrelevant operator, whose coefficient we shall call z :¹⁰

$$G_{\pm}(R) = b^{-y} G_{\pm}(b^{yt}t, b^{yx}x, b^{-1}R, b^{-\omega}z). \quad (\text{D17})$$

Now choosing b as before gives

$$G_{\pm}(R) = x^{y/y_x} G_{\pm}(x^{-yt/y_x}t, 1, x^{1/y_x}R, x^{\omega/y_x}z). \quad (\text{D18})$$

Quantities like A_{\pm} now depend on $x^{\omega/y_x}z$ but, for small x , can be Taylor expanded:

$$\frac{\xi_+}{\xi_-} = \frac{A_+}{A_-} = O(x^0) \left[1 + O(x^{\omega/y_x}) \right]. \quad (\text{D19})$$

For small or zero α , we should make the replacement (D7) as before, and turn to the second-order RG equation (D13).¹¹ One easily finds that correction-to-scaling laws such as (3.16), which do not explicitly depend on α , remain valid.

¹⁰ Some readers may be more familiar with thinking of the RG flow in the cubic anisotropy model [1–3,7,8], which is in the same universality class, and in terms of the ϵ expansion. The potential energy in that model is of the form $u(\phi_1^2 + \phi_2^2)^2 + v(\phi_1^4 + \phi_2^4)$. Roughly speaking, z here corresponds to v and x to a linear combination of $-u$ and v .

¹¹ There will in general also be a term $c'\bar{x}\bar{z}$ on the right-hand side of (D13) but, because z is irrelevant, this term quickly becomes negligible as b is increased and does not affect any of our conclusions.

REFERENCES

- [1] P. Arnold, S. Sharpe, L. Yaffe and Y. Zhang, University of Washington preprint UW/PT-96-25 (in preparation).
- [2] P. Arnold and L. Yaffe, University of Washington preprint UW/PT-96-23, hep-ph/9610447; P. Arnold and Y. Zhang, University of Washington preprint UW/PT-96-24, hep-ph/9610448.
- [3] J. Rudnick, Phys. Rev. B **11**, 3397 (1975).
- [4] J. Ashkin and E. Teller, Phys. Rev. **64**, 178 2542 (1943).
- [5] F. Wu, Rev. Mod. Phys. **54**, 235 (1982).
- [6] R. Ditzian, J. Banavar, G. Grest, L. Kadanoff, Phys. Rev. B **22**, 2542 (1980).
- [7] A. Aharony in *Phase Transitions and Critical Phenomena: Vol. 6*, eds. C. Domb and M. Green (Academic Press, 1976), 357.
- [8] M. Alford and J. March-Russell, Nucl. Phys. **B417**, 527 (1994).
- [9] I. Ono and K. Ito, J. Phys. C **15**, 4417 (1982).
- [10] S. Ohta, Nucl. Phys. B (Proc. Suppl.) **34**, 279 (1993).
- [11] D. Kim and R. Joseph, J. Phys. A **8**, 891 (1975).
- [12] R. Ditzian and L. Kadanoff, J. Phys. A **12**, L229 (1979).
- [13] U. Wolff, Phys. Rev. Lett. **62**, 361 (1989).
- [14] C. Baillie, R. Gupta, K. Hawick, G. Pawley, Phys. Rev. B **45**, 10438 (1992).
- [15] G. Baker, B. Nickel, M. Greaan, and D. Meiron, Phys. Rev. Lett. **36**, 1351 (1976); G. Baker, B. Nickel, and D. Meiron, Phys. Rev. B **17**, 1365 (1978); J. Le Guillou and J. Zinn-Justin, Phys. Rev. Lett. **39**, 95 (1977); Phys. Rev. B **21**, 3976 (1980).

- [16] See, for example, N. Madras and A. Sokal, *J. Stat. Phys.* **50**, 109 (1988); I. Montvay and G. Münster, *Quantum Field on a Lattice* (Cambridge University Press, 1994).
- [17] See, for example, M. B. Priestley, *Spectral Analysis and Time Series* (Academic Press, 1981); T. W. Anderson, *The Statistical Analysis of Time Series* (Wiley, 1971)
- [18] R. Swendsen and J. Wang, *Phys. Rev. Lett.* **58**, 86 (1987).
- [19] S. Wiseman and E. Domany, *Phys. Rev. E* **48**, 4080 (1993).
- [20] J. Salas and A. Sokal, *J. Stat. Phys.* **85**, 297 (1996).